Discovery and Design of Next Generation Inhibitors Targeting the HER2/HER3 heterodimer and K-Ras

by

Chris J. Novotny

DISSERTATION

Submitted in partial satisfaction of the requirements for the degree of

DOCTOR OF PHILOSOPHY

in

Chemistry and Chemical Biology

in the

GRADUATE DIVISION

of the

UNIVERSITY OF CALIFORNIA, SAN FRANCISCO

Acknowledgements

I would like to thank my advisor Dr. Kevan Shokat for giving me the freedom and encouragement to pursue challenging problems in addition to providing advice and guidance. My Thesis committee members Dr. Jack Taunton and Dr. William Weiss for helpful conversations and their ideas. Many members of the Shokat lab both past and present whose influence has shaped the scientist I am today. Flora Rutaganira whose support and kindness was instrumental in helping me get through grad school. And my parents, who throughout my life have given me all of the opportunities necessary for me to make it this far while providing constant love and support.

Part of this thesis is a reproduction of material previously published and contains contributions from collaborators listed therein. Chapter 1 is reproduced in part with permission from Novotny, C.J., Pollari, S., Park, J.H., Lemmon, M.A., Shen, W., Shokat, K.M. (2016). Overcoming Resistance to HER2 Inhibitors Through State-Specific Kinase Binding. *Nature Chemical Biology*, In press. Chapter 2 is reproduced in part with permission from Novotny, C.J.*, Hamiltion, G.*, Shokat, K.M. Farnesyltransferase-mediated Delivery of a Covalent Inhibitor Overcomes Alternative Prenylation to Mislocalize K-Ras. *In preparation*.

Discovery and Design of Next Generation Inhibitors to Targeting the HER2/HER3 Heterodimer and K-Ras

Chris J. Novotny

Abstract

Targeted inhibitors of driving oncogenes impose a selective pressure that benefits those cells who can most quickly and efficiently bypass the insult. While much attention, particularly in the kinase inhibitor field, has focused on the selective outgrowth of cells harboring mutations that directly impact the inhibitors ability to bind a much more rapid innate resistance mechanism often exists that it is revealed by the presence of the inhibitor. In chapter 1 we found that growth factor driven resistance to current clinical HER2 inhibitors was due to the inability of the inhibitors to directly target the active state of the kinase. We used this information to design a screen for an inhibitor of the active HER2/HER3 complex resulting in the identification of one hit scaffold. Optimization of our small molecule hit resulted in a HER2 inhibitor that was insensitive the presence of growth factor and also capable of targeting the mutationally activated form of HER2. In chapter 2 we used the existing known biology of K-Ras's ability to bypass first generation farnesyltransferase inhibitors to design an inhibitor that would simultaneously block K-Ras cellular localization and its ability to bypass inhibition. The resulting inhibitor was found to block K-Ras localization in cells, and when combined with statins, was found to inhibit oncogenic K-Ras signaling and proliferation.

Table of Contents

Chapter 1 Overcoming Resistance to HER2 Inhibitors Through State Specific Kinase Binding 1

Abstract 2

Introduction 2

HER2/HER3 Heterodimers are Resistant to Current Inhibitors 5

Identification of a Novel HER2/HER3 Inhibitor 10

The Cellular Activity of **2** Results from HER2 Inhibition 14

Type I HER2 Inhibitors are Insensitive to NRG Stimulation 20

Discussion 30

Methods 32

References 47

Chapter 2 Farnesyltransferase-mediated Delivery of a Covalent Inhibitor Overcomes Alternative Prenylation to Mislocalize K-Ras 52

Abstract 53

Introduction 53

Design and activity of electrophilic farnesyltransferase inhibitors of K-Ras 56

6* Mislocalizes m-Cerulean K-Ras (G12C) 58

6* Prevents K-Ras bypass of FTase and Mislocalizes K-Ras 61

Discussion 64

Methods 65

References 69

Chapter 3 Design of a Novel HER3 Binder 74

Methods 83

References 93

List of Tables

Table 1.1	Complete profiling of **2** at 100nM conducted by Nanosyn	16
Table 1.2	Complete profiling of **2** at 1 μM conducted by Nanosyn	17
Table 1.3	IC_{50} Values for Gatekeeper mutant 2YF/3 containing Ba/F3 Cells	20
Table 1.4	Complete profiling of **3** at 1 μM conducted by Nanosyn	20
Table 1.5	IC_{50} Values for HER2 mutant 2YF/3 containing Ba/F3 Cells	28

List of Figures

Fig. 1.1	NRG Rescues HER2-overexpressing cancer cells from lapatinib	5
Fig. 1.2	NRG Rescues HER2-overexpressing cells proliferation from TAK-285	6
Fig. 1.3	Within the EGFR family NRG only Rescues HER3 signaling	6
Fig. 1.4	Lapatinib is unable to bind to the active HER2/HER3 heterodimer	8
Fig. 1.5	NRG pre-treatment rescues HER2/HER3 signaling from lapatinib	9
Fig. 1.6	Design and execution of a high-throughput screen identifies a novel HER2/HER3 inhibitor	13
Fig. 1.7	MAPK and mTOR Inhibitor controls for Ba/F3 screening line	14
Fig. 1.8	Compound **2** is a selective Type I inhibitor or HER2	15
Fig. 1.9	Mutation of the gatekeeper residue of HER2 or HER3 to methionine reduces the binding affinity of **2**	19
Fig. 1.10	A type I inhibitor of HER2 is insensitive to the presence of NRG	22
Fig. 1.11	*In vitro* kinase assay of the HER2 kinase domain against **3**	22
Fig. 1.12	SK-BR-3 cells treated with a dose response of **3** in the presence or absence of NRG for 1h.	23
Fig. 1.13	NRG rescues HER2 overexpressing cell lines from DFG in/α-C out inhibitors but not **3**	24
Fig. 1.14	**3** does not disrupt the HER2/HER3/NRG complex	24
Fig. 1.15	**3** binds active HER2 in MCF-7 cells	25
Fig. 1.16	**3** binds to active HER2 in SK-BR-3 pre-treated with NRG	25
Fig. 1.17	NRG rescues HER3 mutant drive Ba/F3 cells from DFG in/α-C out inhibitors but not **3**	26
Fig. 1.18	**3** inhibits the active HER2/HER3 heterodimer in multiple oncogenic settings	27
Fig. 1.19	**3** is a more potent inhibitor of CHL-1 cell growth	29
Fig. 1.20	FaDu cells are more sensitive to **3** compared to lapatinib	29

Fig. 1.21	Pharmacokinetics of **3**	30
Fig. 2.1	Proposed method to overcome innate resistance to K-Ras PTM inhibition	55
Fig. 2.2	Design and *in vitro* activity of eFTI	57
Fig. 2.3	**6*** displaces K-Ras(G12C) from the plasma membrane	59
Fig. 2.4	Representative example of the values taken to calculate the cytoplasmic and membrane fluorescence for a cell treated with either DMSO or **6***	60
Fig. 2.5	**6*** mislocalizes oncogenic K-Ras into the cytoplasm	61
Fig. 2.6	**6*** is active against other oncogenic variants of K-Ras	62
Fig. 2.7	**6*** in combination with statins can inhibit K-Ras signaling and proliferation	63
Fig. 3.1	Hybrid HER3 binder structures and activity in HER3 melting assay	76
Fig. 3.2	Crystal structure of **179D** bound to EGFR	77
Fig. 3.3	Chemical structure and HER3 melting curve for **50A**	78
Fig. 3.4	HER3 binders fail to alter HER3 signaling in CHL-1 cells	79
Fig. 3.5	Chemical structure and HER3 melting curve for extended type II binders	80
Fig. 3.6	Crystal structure of **73** bound to EGFR	81
Fig. 3.7	Chemical structure **87** and western blot of CHL-1 cells treated with **87**	82
Fig. 3.8	Chemical structure of **8003** and western blot of HEK cells treated with **8003**	82

Chapter 1:

Overcoming Resistance to HER2 Inhibitors Through State-Specific Kinase Binding

Abstract

The heterodimeric receptor tyrosine kinase complex formed by HER2 and HER3 can act as an oncogenic driver and is also responsible for rescuing a large number of cancers from a diverse set of targeted therapies. Current inhibitors of these proteins, particularly HER2, have dramatically improved patient outcomes in the clinic but recent studies have demonstrated that stimulation of the heterodimeric complex, either by growth factors or increasing the concentrations of HER2 and HER3 at the membrane, significantly diminishes their activity. In order to find an inhibitor of the active HER2/HER3 oncogenic complex we developed a panel of Ba/F3 cell lines suitable for ultra-high throughput screening. Medicinal chemistry on the hit scaffold resulted in a novel inhibitor that acts through the preferential inhibition of the active state of HER2 and as a result is able to overcome cellular mechanisms of resistance such as growth factors or mutations that stabilize the active form of HER2.

Introduction

Signaling from the epidermal growth factor receptor (EGFR or HER) family of receptor tyrosine kinases (RTK) is dependent on a well-orchestrated series of interactions between family members to form either homo- or heterodimers[1-3]. This dimerization process allows the intracellular kinase domains to form an asymmetric dimer in which the C-terminal domain of the activator kinase binds to the N-terminal portion of the receiver kinase to stabilize it in an active conformation[4](Fig. 1.1a). The receiver kinase then phosphorylates tyrosine residues on the C-terminal tails of the kinases to recruit and activate downstream signaling components, most notably those involved in pro-growth and survival pathways. As a result, the improper activation of the EGFR family of kinases, either by mutation or overexpression, is observed in a variety of

cancers[5,6]. Interestingly, cell culture studies suggest that rather than causing escape from the biological mechanism of regulation, oncogenic activation alters the equilibrium between active and inactive states to favor the improper dimerization and activation of these receptors[7,8 9]. This dependence on dimerization is particularly evident in HER2-overexpressing breast cancers that are dependent on the presence of HER3[10].

Within the EGFR family, HER2 and HER3 are unique. HER3 is classified as a pseudokinase with only residual kinase activity, whereas HER2 has no known activating ligand but is constitutively able to dimerize with other active family members. In this way, HER2 and HER3 together form a functional RTK unit, with HER3 responding to activating ligands such as neuregulin, HER2 providing the intracellular kinase activity, and both intracellular domains providing phosphorylation sites. Additionally, HER2 and HER3 are each other's preferred heterodimerization partners and also form the most mitogenic complex among all possible EGFR family dimers[11]. Because of this co-dependence, HER3 is equally important for the formation, proliferation, and survival of HER2-overexpressing tumors[12].

Although HER2 amplification and overexpression is the most well studied means of oncogenic activation of the HER2/HER3 heterodimer, improper signaling can also be caused by secretion of the HER3 ligand NRG to stimulate HER2/HER3 heterodimers in an autocrine manner as well as by mutations in HER3 that stabilize and activate heterodimers independently of ligand[13,14]. In addition, mutations that activate the HER2 kinase domain have also been reported[15-17].

In an effort to treat these tumors, small molecule kinase inhibitors such as lapatinib or HER2-targeted antibodies such as ado-trastuzumab emtansine (T-DM1) have been developed and shown efficacy against HER2-driven cancers in the clinic[18,19]. However, recent studies have

demonstrated that the presence of NRG induces resistance against currently approved HER2-targeted mono-therapies through HER2/HER3 signaling[20,21]. Additionally, inhibition of HER2/HER3 signaling at either the RTK level or of the downstream PI3K/Akt pathway releases a negative feedback loop that increases the transcription, translation, and membrane localization of HER3[22-24]. This increase in the level of HER3 causes a rebound in its phosphorylation and reactivation of the PI3K/Akt pathway even in the continued presence of lapatinib, indicating that formation of HER2/HER3 heterodimers is crucial for intrinsic cellular resistance to current HER2-targeted therapies[25]. This severe limitation illustrates why more effective therapies targeting the active HER2/HER3 dimer are required.

Here, we evaluated the ability of current reversible HER2 inhibitors to inhibit signaling and proliferation in cancer cell lines driven by HER2/HER3 heterodimers activated by different oncogenic mechanisms. Across several cell lines, stabilization of HER2 in the active conformation led to severely diminished activity of both lapatinib and TAK-285. We therefore aimed to identify a novel HER2/HER3 inhibitor that would preferentially target the active state of the heterodimer. Reasoning that a biochemical screen would be unable to capture the relevant cellular conformation of the fully formed transmembrane complex, we turned to a cell-based screening strategy. A high throughput screen of 950,000 small molecules against an engineered Ba/F3 cell line dependent on NRG stimulated HER2/HER3 heterodimers yielded a hit scaffold that we optimized to create a next generation HER2 inhibitor. The optimized inhibitor is capable of potently inhibiting signaling from the HER2/HER3 heterodimer regardless of the activating oncogenic mechanism.

Results

HER2/HER3 Heterodimers are Resistant to current Inhibitors

We first confirmed that the addition of the HER3 activating ligand neuregulin 1 (NRG) is able to dramatically rescue the proliferation of HER2-overexpressing breast cancer cell lines treated with the HER2 kinase inhibitors lapatinib and TAK-285 (Fig. 1.1b, 1.2). This rescue of cell proliferation was dose dependent and effective at pM concentrations of NRG in the presence of

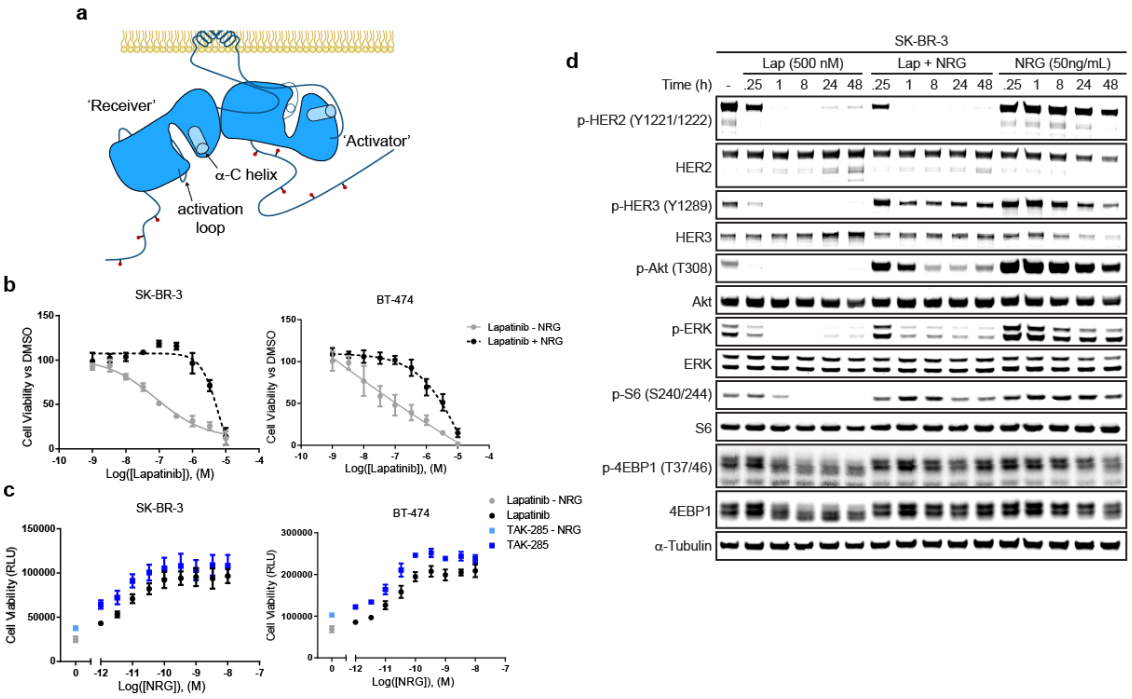

Figure 1.1. NRG rescues HER2-overexpressing cancer cells from HER2 inhibitors. **a.** Cartoon schematic of the EGFR family kinase domain asymmetric dimer. The C-terminal domain of the 'activator' kinase (right) interacts with the N-terminal portion of the 'receiver' kinase (left). This interaction stabilizes the active conformation of the receiver kinase identified by the 'in' conformation of the receiver kinase's α-C helix and the ordered extension of the activation loop. The activator kinase retains the inactive conformation. **b**. 72 h proliferation of SK-BR-3 and BT-474 cells treated with a dose-response of lapatinib in the presence or absence of NRG (mean ± SD, n=3). **c.** The ability of NRG to rescue SK-BR-3 and BT-474 cell proliferation from HER2 inhibitors is dose dependent. Cells were treated with 1 μM of the indicated inhibitor in the presence of varying concentrations of NRG, and proliferation was read out after72h (mean ± SD, n=3). **d.** HER2/HER3 signaling was evaluated over a time-course in SK-BR-3 cells treated with either lapatinib, NRG, or both. The addition of NRG rescues p-HER3 and all downstream signaling at all time points examined.

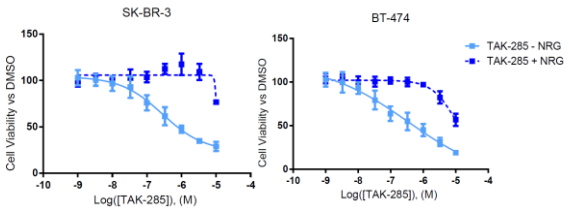

Figure 1.2. 72h proliferation of SK-BR-3 or BT-474 cells treated with a dose-response of TAK-285 in the presence or absence of NRG (mean±SD, n=3).

either HER2 inhibitor at 1 µM (Fig. 1.1c). To determine how NRG was able to so profoundly rescue cellular proliferation, we examined a time course of HER2/HER3 signaling in SK-BR-3 cells exposed to either lapatinib, NRG, or the combination of the two. While lapatinib alone was able to rapidly and sustainably inhibit all signaling from HER2 and HER3, the addition of NRG prevented the complete inhibition of p-HER3 and all downstream signaling pathways at all time points examined (Fig. 1.1d). Analysis of signaling from alternative EGFR family members that could potentially contribute to this phenotype revealed that p-EGFR actually decreased in response to NRG and was still able to be inhibited by lapatinib while HER4, which is thought to function as a tumor suppressor, was undetectable in this cell line (Fig.1.3) [26,27].

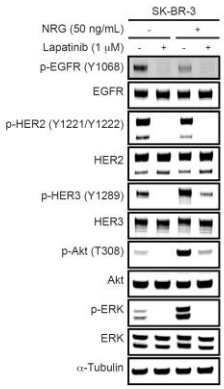

Figure 1.3. SK-BR-3 cells were treated with DMSO or 1 µM lapatinib in the presence or absence of NRG for 1h. HER3 is the only member of the EGFR family who remains activated in the presence of both NRG and lapatinib. HER4 was undetectable in this cell line.

The ability of NRG to rescue HER3 signaling in the presence of lapatinib could have several origins. The very weak kinase activity of HER3 itself is unlikely to be sufficient – although it is not inhibited by lapatinib. A more likely explanation is that NRG-induced heterodimerization of HER2 and HER3 stabilizes a conformation of the HER2 kinase domain that is resistant to the inhibitors tested. Both lapatinib and TAK-285 bind to the DFG in/α-C out kinase conformation and occupy the back hydrophobic pocket of HER2 that is only available when the kinase domain is in an inactive conformation with the αC-helix in the characteristic 'out' position[28,29]. This mode of binding has the advantage of giving these inhibitors slow off-rates but could also explain their ineffectiveness in the presence of NRG. Crystal structures of EGFR family homodimers and of a HER3/EGFR kinase complex have shown that only the 'activator' kinase in the asymmetric dimer can retain the inactive conformation (Fig. 1.1a) [30,31]. In HER2/HER3 complexes, HER3 will adopt this position exclusively, whereas HER2 will take the 'receiver' kinase position and become stabilized in the active conformation. Thus, in a HER2/HER3 complex, the size and accessibility of the back hydrophobic pocket of the HER2 kinase domain will be greatly reduced, preventing lapatinib or TAK-285 from binding.

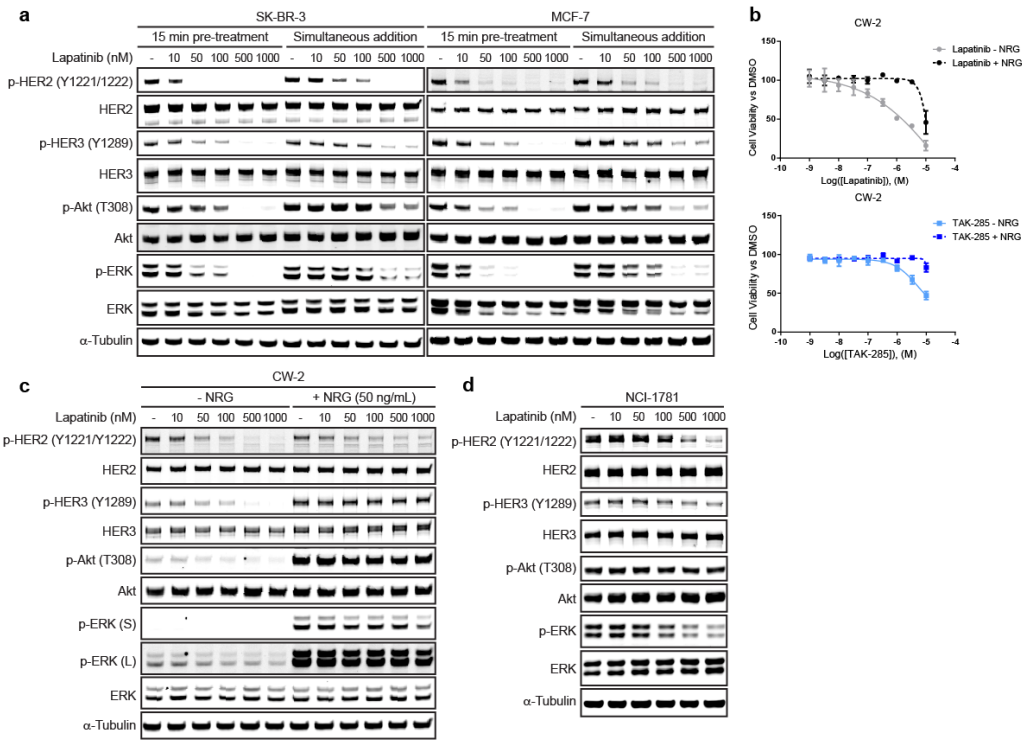

Figure 1.4. . Lapatinib is unable to bind to the active HER2/HER3 heterodimer. **a.** SK-BR-3 or MCF-7 cells were serum starved for 24 h and then either treated with lapatinib alone for 15 min – followed by a 15 min NRG stimulation (50ng/mL) (15 min pre-treat), or were treated with lapatinib and NRG together for 15 min (simultaneous addition). The reduced efficacy of lapatinib when simultaneously added with NRG indicates a reduced ability to bind active HER2 in HER2/HER3 heterodimers. **b.** NRG rescues the 72h proliferation of CW-2 cells from HER2 inhibitors (mean ± SD, n=3). **c**. CW-2 cells treated with a dose response of lapatinib in the presence or absence of NRG (50ng/mL) for 1h show that NRG rescues HER2/HER3 signaling. **d.** NCI-H1781 cells were treated with a dose response of lapatinib, and signaling was evaluated after 15 min. The short treatment time shows lapatinib does not efficiently bind to HER2 mutants biased towards the active conformation.

To determine if NRG-induced heterodimerization prevents lapatinib binding, we treated serum-starved SK-BR-3 cells with lapatinib either 15 min before or simultaneously with NRG stimulation and then rapidly examined HER2/HER3 signaling to monitor the on-rate of lapatinib in these cells. Lapatinib concentrations greater than 100 nM were sufficient to inhibit the entire RTK signaling pathway when added before NRG (Fig. 1.4a), i.e. in the absence of HER2/HER3

heterodimers. By contrast, lapatinib was much less effective when added simultaneously with NRG – where lapatinib would need to bind to the NRG-induced HER2/HER3 heterodimer to inhibit signaling – even at a concentration of 1 μM (Fig. 1.4a). A similar trend was seen in MCF-7 cells, which express modest levels of HER2 and HER3, demonstrating that this effect does not require HER2 overexpression (Fig. 1.4a). The same trend was also observed when cells were first treated with either NRG or vehicle for 15 min followed by 15 min of lapatinib treatment (Supplementary Fig. 1.5).

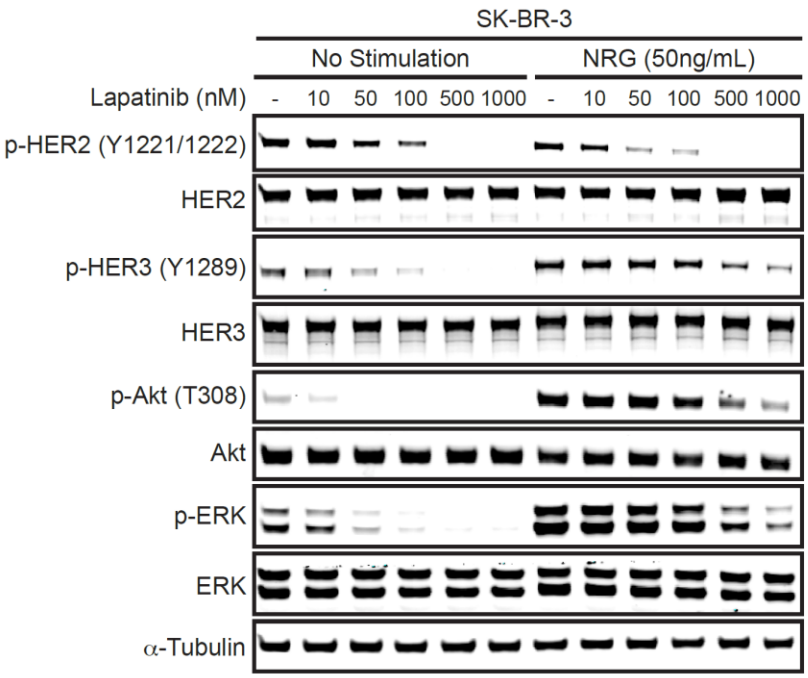

Figure 1.5. NRG pre-treatment rescues HER2/HER3 signaling from lapatinib. SK-BR-3 cells were serum starved for 24h and then either treated with NRG or vehicle for 15 min followed by a dose response of lapatinib for 15 min and signaling was analyzed by western blot.

To assess if NRG's ability to rescue the cellular proliferation of cell lines where the HER2/HER3 dimer may be activated by alternative mechanisms, we assessed signaling and proliferation in CW-2 cells, which contain an activating mutation in the C-lobe of HER3 (E928G)

and in the N-lobe of HER2 (L755S). Similar to the HER2-overexpressing cell lines, the addition of NRG rescued the viability of the CW-2 cells in a 72 h proliferation assay from both HER2 inhibitors and rescued HER2/HER3 signaling from lapatinib (Fig. 1.4b, c).

We next sought to determine whether this apparent resistance to lapatinib is specific to NRG-induced HER2/HER3 heterodimers or if mutations that bias HER2 towards its active conformation elicit a similar effect. We monitored HER2 and HER3 signaling 15 min after the addition of lapatinib in NCI-H1781 cells, which contain an insertion in the HER2 kinase domain at a position known to increase HER2 kinase activity[16]. As shown in Figure 1.4d, lapatinib, even at a concentration of 1 μM, was unable to fully inhibit signaling demonstrating that this activating mutation is sufficient to hinder lapatinib binding to HER2.

Taken together, these data argue that NRG rescues HER2/HER3 driven cells from DFG in/α-C out inhibitors by stabilizing HER2 in the active conformation within HER2/HER3 heterodimers. This inability to directly target the active state of HER2 places a major limitation on the effectiveness of a majority of current HER2 inhibitors since inhibition of HER2/HER3 signaling triggers feedback loops that lead to the increased membrane expression of HER2 and HER3, which increases the number of active HER2/HER3 heterodimers that then rescue signaling and proliferation[22,23,25]. Our findings therefore argue that inhibitors that target the active HER2/HER3 heterodimer will have significant advantages, especially in situations that increase the number of active HER2/HER3 heterodimers.

Identification of a Novel HER2/HER3 Inhibitor

In order to find a small molecule inhibitor capable of binding to the active HER2/HER3 signaling complex we developed a high throughput cellular screen using a Ba/F3 cell line engineered to be dependent on NRG-induced HER2/HER3 heterodimers. Ba/F3 cells are

normally dependent on IL-3 signaling for their proliferation and survival but can be made dependent on introduced oncogenic signals[32]. We sequentially selected transduced Ba/F3 cells for populations stably expressing HER3 and then HER2. To ensure that all of the proliferative signal could be attributed to HER2/HER3 heterodimers rather than HER2 homodimers, the 9 C-terminal tyrosines in HER2 were mutated to phenylalanine (HER2YF). We then withdrew IL-3 and supplemented the media with NRG to select for NRG dependent HER2YF/HER3wt cells (2YF/3wt). The resulting 2YF/3wt cell line was completely dependent on NRG for survival and allowed us to screen for inhibitors of full-length HER2/HER3 heterodimers in their native cellular conformations using a cell viability assay (Fig. 1.6a). In addition to allowing us to identify potential inhibitors of active HER2, this cellular system also has the potential to uncover compounds with novel mechanisms of action against the pseudokinase HER3.

To validate the screen and test the effectiveness of counter-screening with either the same 2YF/3wt Ba/F3 cell line or the parental Ba/F3 cell line in the presence of IL-3 to remove cytotoxic primary hits, we first tested a panel of kinase inhibitors with established mechanisms of action. This panel of inhibitors demonstrated that MAPK pathway inhibitors (e.g. vemurafenib) would not score as hits in NRG-treated 2YF/3wt cells, whereas mTOR inhibitors (e.g. MLN0128) are ruled out in our toxicity counter screen, showing equal activity in the presence of either NRG or IL-3 (Fig. 1.7). By contrast, HER2 and PI3K inhibitors showed a clear window for selective inhibition of NRG driven cells over IL-3 driven cells (Fig. 1.6b). In order to rapidly remove any hit compound that did not directly target the HER2/HER3 heterodimer, we created a separate Ba/F3 cell line dependent on the overexpression of full-length wt Axl, which also signals through the PI3K pathway. As shown in Figure 1.6b, this panel of Ba/F3 cell lines was suitable to segregate lapatinib from the PI3K inhibitor PIK-93.

The 48 h proliferation assay of 2YF/3wt + NRG cells was miniaturized and optimized for 1,536-well plates, which we used to screen a diverse collection of 950,000 drug-like molecules (Z' ≥0.75). This primary screen resulted in 14,012 hits (>50% inhibition vs DMSO) that were reduced to 1,423 compounds after triplicate confirmation and the parental Ba/F3 + IL-3 counter-screen (<30% inhibition vs DMSO). These 1,423 compounds were then assayed in dose response against all three cell lines (2YF/3wt + NRG, parental Ba/F3 + IL-3, and Axl+) (Fig. 1.6c,). This screening and triaging process led to the identification of three hit compounds sharing the same scaffold, exemplified by compound **1** in Fig. 1.6d, which reproducibly showed preferential inhibition of 2YF/3wt + NRG cell proliferation. Optimization of the hit scaffold through five iterations of analog synthesis, each consisting of approximately ten compounds, led to compound **2**, which shows a marked preference for the inhibition of the NRG driven cells over the others (Fig. 1.6e).

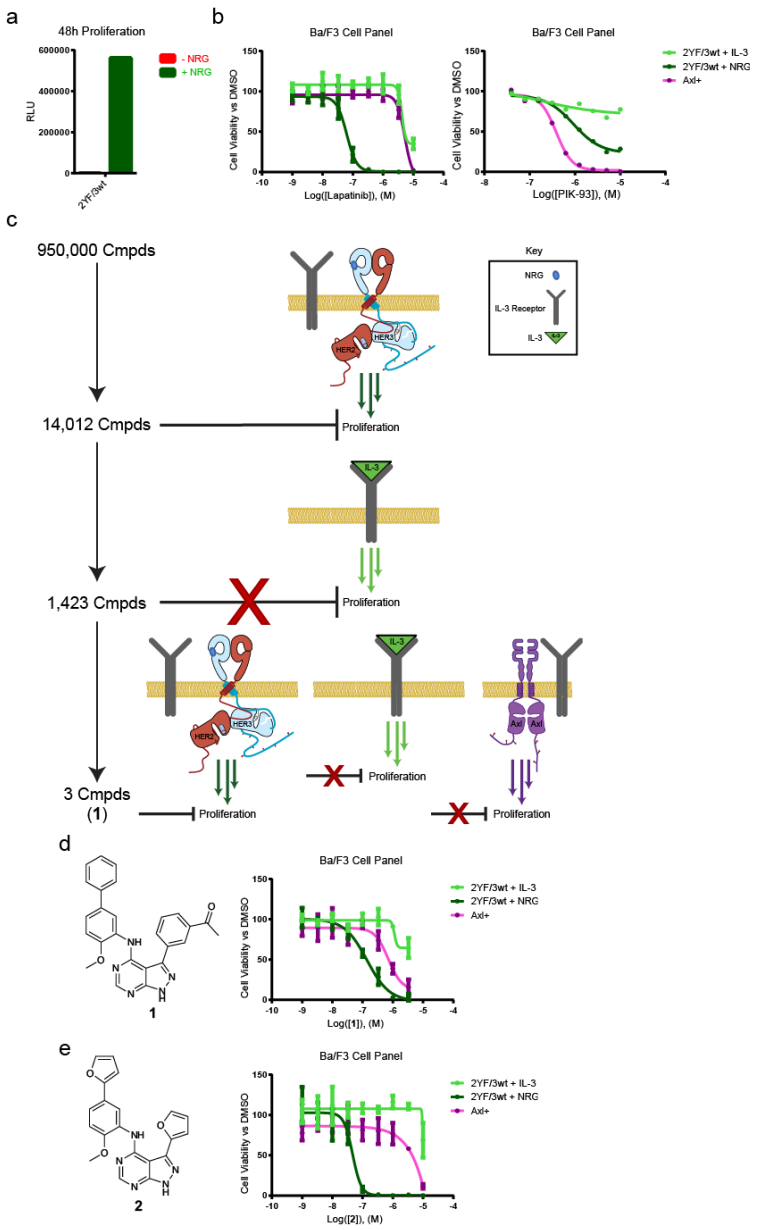

Figure 1.6. Design and execution of a high-throughput screen identifies a novel HER2/HER3 inhibitor. **a**. 2YF/3wt cells were incubated in the presence or absence of NRG for 48h and proliferation was assessed by CellTiter-Glo (mean, n=1). **b**. 48h proliferation curves of the Ba/F3 cell panel show they can separate out compounds that specifically inhibit signaling at the HER2/HER3 level (lapatinib) from those that hit downstream (PIK-93) (for lapatinib mean ± SD, n=3, for PIK-93 mean, n=1). **c**. A schematic of the high throughput screen. Compounds were first screened for the ability to inhibit the proliferation of the 2YF/3wt + NRG cells, counter-screened against the parental cells in the presence of IL-3, and then screened in dose response against all 3 cell lines. **d.** Structure and proliferation curves for hit compound **1** against the Ba/F3 cell line

panel (mean ± SD, n=3). **e.** Structure and proliferation curves for compound **2** against the panel of Ba/F3 cell lines (mean ± SD, n=3).

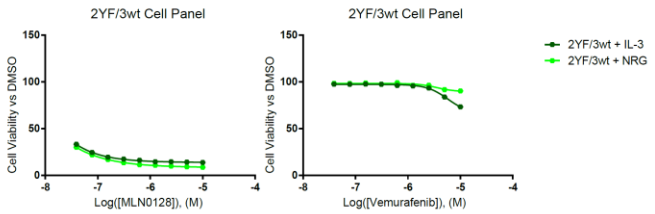

Figure 1.7. 48h proliferation curves of the 2YF/3wt Ba/F3 cell line in the presence of either NRG or IL-3 (mean, n=1).

The Cellular Activity of 2 Results from HER2 Inhibition

The specificity of compound **2** for the NRG-driven 2YF/3wt cells indicated that the compound had reasonable kinase specificity and was likely interfering with signaling at the RTK level. This was confirmed by *in vitro* profiling against a panel of kinases, with **2** only showing potent inhibition of EGFR and Abl (Table 1.1, 1.2). To determine the mechanism of action of **2**, we evaluated its ability to interact with HER2 or HER3 using an *in vitro* kinase assay or thermofluor respectively. Compound **2** was equipotent to lapatinib against HER2 *in vitro* (Fig. 1.8a) and, surprisingly, was also capable of binding to HER3 (Fig. 1.8b). Moreover, unlike all other EGFR family inhibitors examined so far, **2** was also able to inhibit the small amount of HER3 auto-phosphorylation seen when the purified HER3 intracellular domain is clustered, indicating that it binds to the HER3 active site.

To determine how **2** is able to interact with multiple members of the EGFR family, we determined the X-ray crystal structure of **2** bound to the EGFR kinase domain (Fig. 1.8c). The V924R kinase domain crystallizes in the inactive (autoinhibited) conformation in the absence of inhibitor or when bound to the type I EGFR inhibitor erlotinib, because this mutation places a polar arginine side-chain in the middle of the hydrophobic patch used to form the asymmetric

dimer required for EGFR dimerization[33,34] (Fig. 1.8c). Strikingly, **2** was able to stabilize the active conformation of this mutated EGFR kinase domain in crystals, as evidenced by the "in" conformation of the α-C helix, which allows formation of the characteristic salt-bridge between the β3 lysine and the α-C glutamate, as well as the ordered extension of the activation loop (Fig. 1.8c, d). This finding

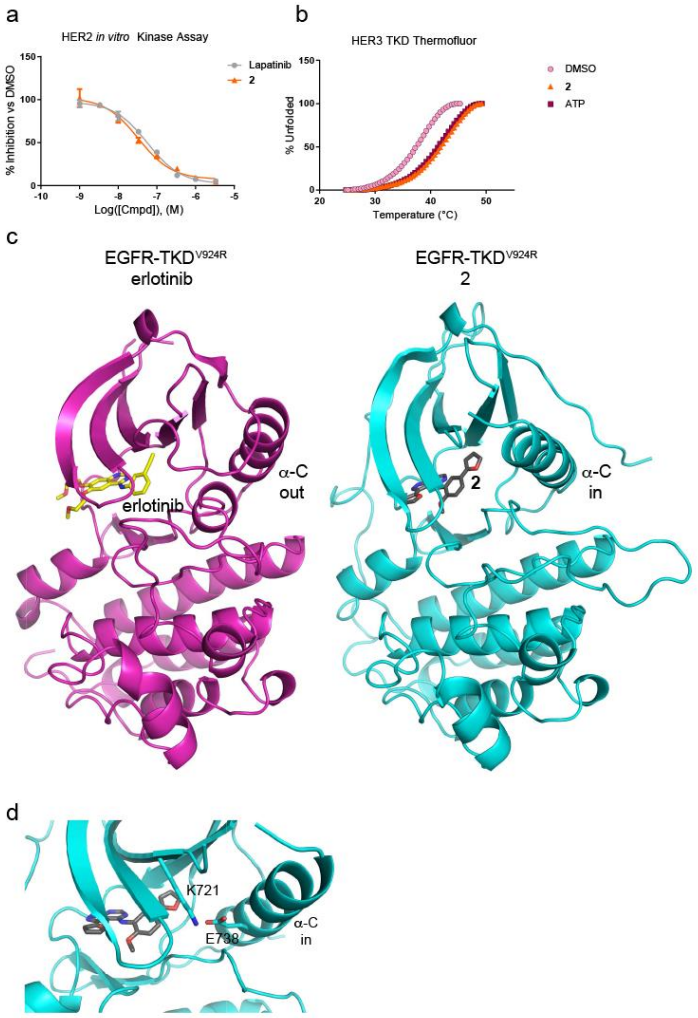

Figure 1.8. Compound **2** is a selective Type I inhibitor or HER2. **a.** *In vitro* kinase assay of the HER2 kinase domain against lapatinib and **2** (mean ± SD, n=3). **b**. Thermal stabilization of the

HER3 kinase domain by either **2** or ATP as determined by thermofluor (mean, n=2). **c.** The crystal structure of either erlotinib (left, PDB:4HJO) or **2** (right) bound to EGFR V924R. The kinase domain in complex with **2** has been stabilized in the active confirmation by drug binding, despite the inactivating mutation – as evidenced by the ordered extension of the activation loop and the inward positioning of the α-C helix. **d.** Magnified view of the EGFR V924R active site when bound to **2** shows the proximity of the β3 lysine (K721) and the glutamate (E738) in the α-C helix, which are positioned so as to make a predicted hydrogen bond.

indicates that our hit scaffold may have a strong preference for binding and stabilizing the active conformation of EGFR family kinase domains. Interestingly, the HER3 kinase domain has only ever been crystallized in the inactive conformation and failed to crystallize after introducing mutations designed to destabilize the inactive state or in the presence of **2** [35,36]. This suggests that **2** may be stabilizing an alternate HER3 kinase domain conformation that could potentially prevent its ability to allosterically activate HER2.

Table 1.1 Complete profiling of **2** at 100nM conducted by Nanosyn.

Kinase	**% Inhibition**
EGFR	95.595
ABL1	95.195
LCK	74.16
SRC	63.24
FLT-3	59.99
BLK	59.895
FGFR1	48.3
MAP4K4	36.53
KDR	27.32
GSK-3-BETA	20.465
JAK3	20.43
TRKC	15.655
SGK1	14.44
AKT1	14.27
IGF1R	13.315
TIE2	12.835
PDGFR-ALPHA	11.85
AURORA-A	9.945
P70S6K1	8.875
CSK	6.955

Kinase	% Inhibition
P38-ALPHA	6.605
ALK	6.145
PRKD2	5.465
DYRK1A	5
PDK1	4.58
CDK2	4.145
PIM-1-KINASE	4.075
DYRK1B	4.01
MST1	3.855
PYK2	3.805
CK1-EPSILON	3.45
EPH-B4	3.44
TYRO3	3.29
AMP-A1B1G1	2.685
EPH-A2	2.42
TRKA	2.385
MET	2.045
IKK-BETA	1.915
NEK2	1.53
IRAK4	1.465
ITK	1.24
PKC-ALPHA	1.24
JNK2	1.075
CHEK1	0.965
TSSK1	0.665
ROCK1	0.155
MAPKAPK-2	0.12
PAK2	0.085
DAPK1	-0.52
SYK	-2.115

Table 1.2 Complete profiling of **2** at 1 µM conducted by Nanosyn

Kinase	% Inhibition
ABL1	97.22
EGFR	96.945
LCK	93.57
BLK	90.405
FLT-3	89.42

Kinase	% Inhibition
SRC	88.935
FGFR1	86.27
MAP4K4	78.705
KDR	71.28
JAK3	69.355
GSK-3-BETA	68.82
TIE2	59.745
SGK1	53.445
IGF1R	53.275
PDGFR-ALPHA	52.5
AURORA-A	47.18
TRKC	46.91
P70S6K1	38.41
AKT1	33.05
PRKD2	26.63
CSK	24.82
CK1-EPSILON	24.12
DYRK1B	22.625
EPH-B4	21.67
EPH-A2	20.97
PYK2	20.195
MST1	19.93
ALK	19.825
PDK1	18.29
CDK2	17.555
DYRK1A	16.68
ITK	13.945
AMP-A1B1G1	12.91
P38-ALPHA	12.91
MET	10.14
PIM-1-KINASE	8.705
JNK2	6.62
PKC-ALPHA	5.57
TYRO3	5.56
TRKA	4.495
NEK2	2.985
IKK-BETA	2.91
CHEK1	2.265
DAPK1	1.425
IRAK4	1.42

Kinase	% Inhibition
ROCK1	1.16
PAK2	1.07
MAPKAPK-2	0.575
TSSK1	-3.06
SYK	-6.41

In order to determine whether binding to HER2, HER3, or to both, was responsible for the anti-proliferative activity of **2,** we created a series of Ba/F3 cell lines dependent on NRG-induced HER2/HER3 heterodimers that possessed methionine gatekeeper mutations (TM) in either kinase alone (2YF/3**TM** and 2YF**TM**/HER3wt) or together (2YF**TM**/3**TM**). The methionine gatekeeper mutation has been shown to prevent lapatinib from binding to HER2 and was able to reduce the ability of **2** to bind to either kinase in isolation (Fig. 1.9) [37]. Consistent with previous reports, both lapatinib and gefitinib (an EGFR inhibitor capable of inhibiting HER2 to a lesser extent) were unable to inhibit the proliferation of either Ba/F3 cell line that contained the gatekeeper mutation in HER2. Similarly, inhibition by **2** was only affected by the HER2 gatekeeper mutation, whereas the gatekeeper mutation in HER3 had little influence (Table 1.3). These data indicate that the cellular activity of **2** is due to inhibition of HER2 kinase activity.

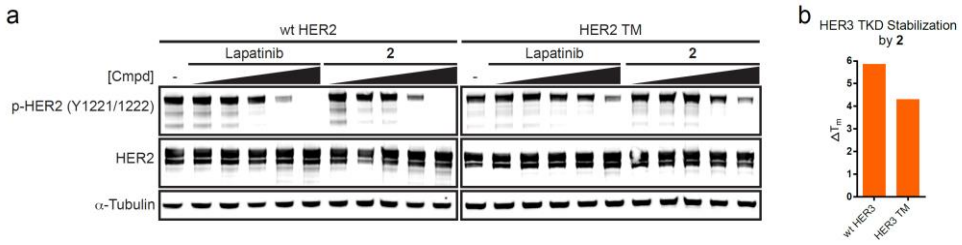

Figure 1.9. Mutation of the gatekeeper residue of HER2 or HER3 to methionine reduces the binding affinity of **2**. **a**.HEK-293T cells were transfected with either wt HER2 or HER2 T798M, which were then treated with a dose response of lapatinib or **2** (1nM – 10μM). **b**. Stabilization of either wt or T787M HER3 kinase domain by **2** compared to DMSO as determined by thermofluor (mean, n=2).

Table 1.3 Table of IC_{50} values (mean ± S.D., n=2)

IC_{50} of Gatekeeper Mutant Ba/F3 Cells Lines (nM ± SD)				
	2YF/3wt	2YF/3**TM**	2YF**TM**/3wt	2YF**TM**/3**TM**
Lapatinib	63.6 ± 12.5	27.8 ± 5.6	>10,000	>10,000
Gefitinib	195.8 ± 36.3	125 ± 52.6	>10,000	>10,000
2	20.0 ± 6.4	18.6 ± 5.9	3,237 ± 415	3,526 ± 797

Type I HER2 Inhibitors are Insensitive to NRG stimulation

Reasoning that a type I inhibitor of HER2 could possess the necessary attributes to inhibit signaling from the active HER2/HER3 heterodimer, we set out to further optimize the potency of our inhibitor. The crystal structure suggested that the extra-cyclic NH linker could form an intramolecular hydrogen bond with the 2-furan, which would help to stabilize the inhibitor in a conformation necessary for binding to the active kinase. The structure also suggested that limiting the charge density on the other 2-furan ring would prevent negative interactions with the kinase. With these parameters in mind, the second optimization effort led to compound **3**, which showed superior activity to lapatinib in the 2YF/3wt + NRG cells and specificity for this cell line over the others by multiple orders of magnitude (Fig. 1.10a, b). *In vitro* kinase profiling of **3** revealed a similar profile to **2** as well as similar potency against HER2 (Table 1.4, Fig. 1.11).

Table 1.4. Complete profiling of **3** at 1 μM conducted by Nanosyn

Kinase	**% inhibition**
MAP4K4	100
EGFR	99
ABL1	98
LCK	98
SRC	95
FGFR1	93
MST1	84
MST2	84

Kinase	% Inhibition
JAK2	83
FLT-3	78
KDR	74
MEK2	70
MEK1	66
PDGFR-ALPHA	66
CSK	62
JAK1	52
TYK2	51
IGF1R	46
DYRK1A	41
PYK2	41
GSK-3-BETA	40
SYK	35
IRAK4	34
AURORA-A	31
SGK1	31
PKC-ALPHA	30
EPH-A2	28
PRKD2	28
ITK	24
AMP-A1B1G1	20
PRKACA	20
CDK1	18
MET	16
ROCK1	16
CK1-EPSILON	11
CDK2	10
CHEK1	10
IKK-BETA	8
JNK2	7
PIM-1-KINASE	7
PI3K-ALPHA	6
PDK1	5
PAK2	3
P38-ALPHA	2
CAMK4	0
DAPK1	-1
MAPK1	-2

Kinase	% Inhibition
MAPKAPK-2	-6
NEK2	-9
FAK	-10

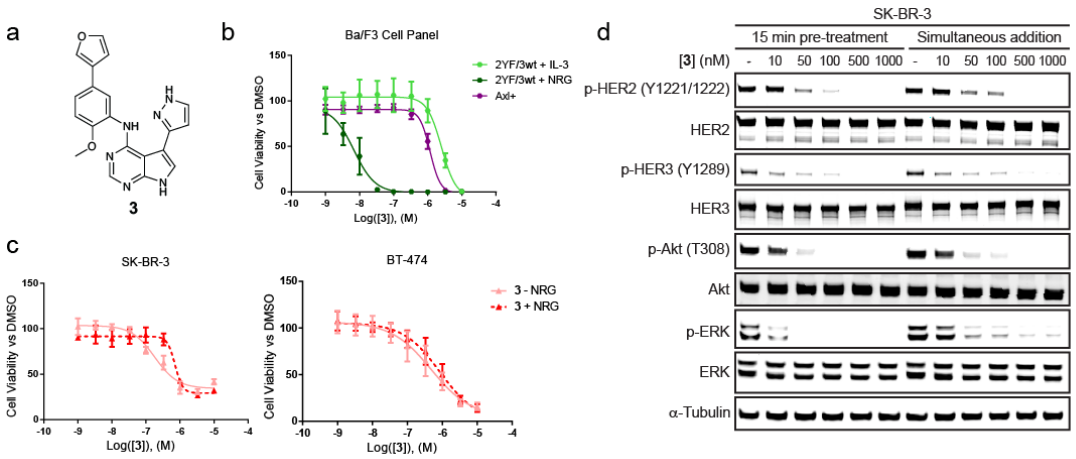

Figure 1.10. A type I inhibitor of HER2 is insensitive to the presence of NRG **a.** Chemical structure of compound **3**. **b**. Proliferation curves for **3** against the Ba/F3 cell line panel (mean ± SD, n=3). **c**. 72h proliferation curves of SK-BR-3 and BT-474 cells treated with a dose response of **3** in the presence or absence of NRG indicates that **3** is insensitive to the presence of NRG in HER2-overexpressing cell lines (mean ± SD, n=3). **d**. The same assay in Fig. 2a was performed with **3** in SK-BR-3 cells.

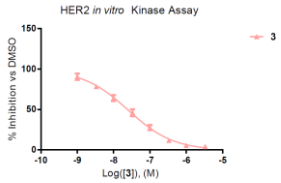

Figure 1.11. *in vitro* kinase assay of the HER2 kinase domain against **3** (mean ± SD, n=3).

Consistent with our hypothesis that a potent type I inhibitor of HER2 would be unaffected by the presence of NRG, **3** showed little to no shift in its ability to inhibit the growth or signaling of HER2-overexpressing cell lines in the presence of NRG (Fig. 1.10c, 1.12). Additionally, unlike lapatinib and TAK-285, 1 µM **3** was able to inhibit the proliferation of HER2-overexpressing cells over a dose response of NRG and was also able to induce cell death in the

presence of NRG (Fig. 1.13). To confirm that **3** could bind to the actively signaling HER2/HER3 heterodimer, we looked at signaling 15 min after the addition of NRG in SK-BR-3 cells either pre-treated with **3** followed by NRG stimulation or simultaneously treated with **3** and NRG. The minimal influence of NRG on the ability of **3** to inhibit all levels of signaling with or without pre-incubation, especially when compared to lapatinib (compare Fig. 1.10d to 1.4a), suggests that it is capable of binding to and inhibiting the active HER2/HER3 complex, which is not disrupted by **3** (Fig. 1.10d, 1.14). A similar result was obtained in non-HER2-amplified MCF-7 cells and when NRG or vehicle was added prior to a dose response of **3** (Fig. 1.15, 1.16).

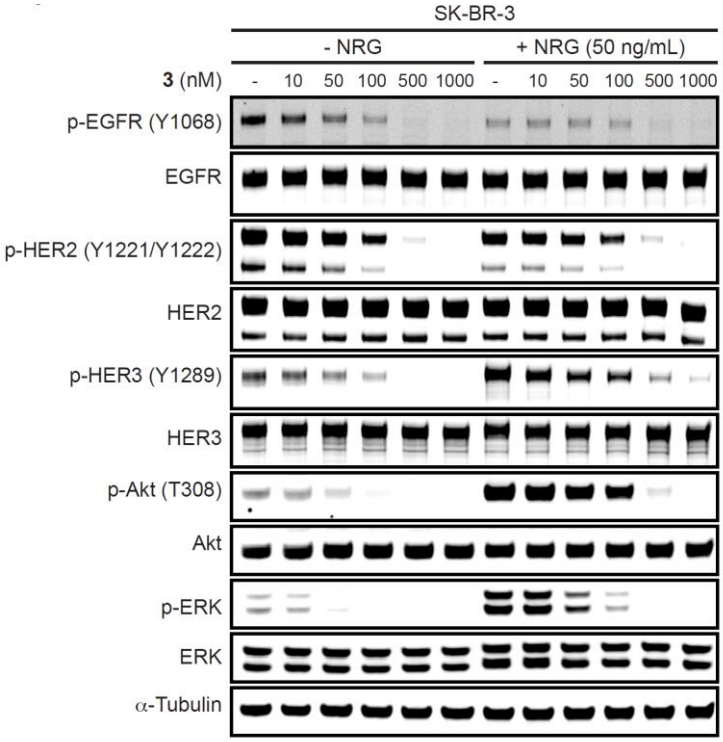

Figure 1.12. SK-BR-3 cells treated with a dose response of **3** in the presence or absence of NRG for 1h.

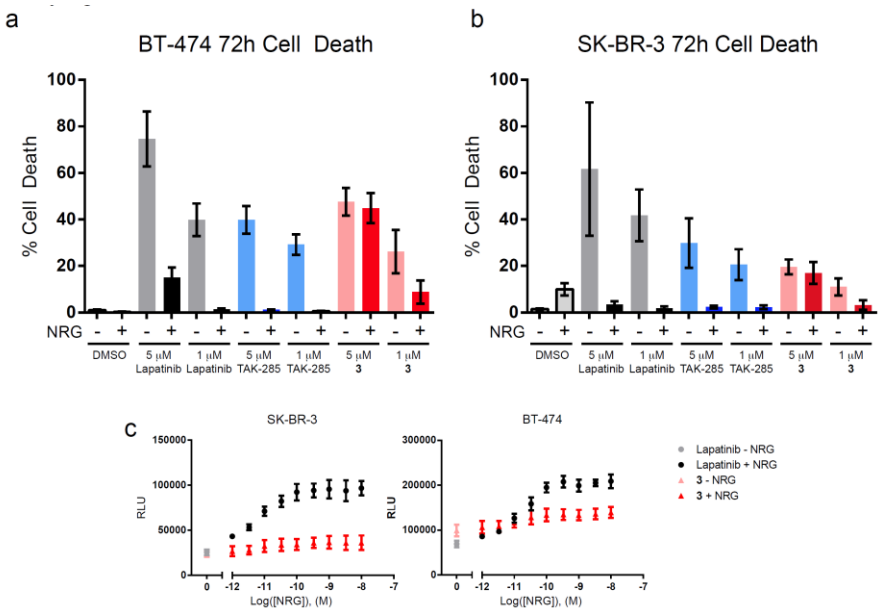

Figure 1.13. NRG rescues HER2 overexpressing cell lines from DFG in/α-C out inhibitors but not **3**. **a**. BT-474 cells were treated with the indicated concentrations of drugs in the presence or absence of NRG for 72h. Cell death was determined using CellTox green with the incucyte Zoom. (mean ± SD, n=3). **b**. Same experiment as in **a** but with SK-BR-3 cells. **c**. Cells were treated with 1 μM of the indicated inhibitor in the presence of varying concentrations of NRG. The lapatinib data is reproduced from figure 1.1c and is shown for reference (mean ± SD, n=3).

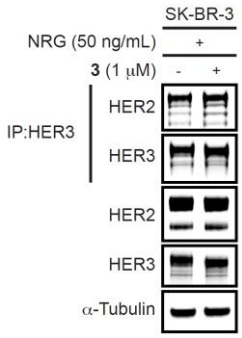

Figure 1.14. SK-BR-3 cells were treated with NRG +/- 1 μM of **3** for 1h. HER3 was purified by immunoprecipitation and analyzed for the presence of HER2.

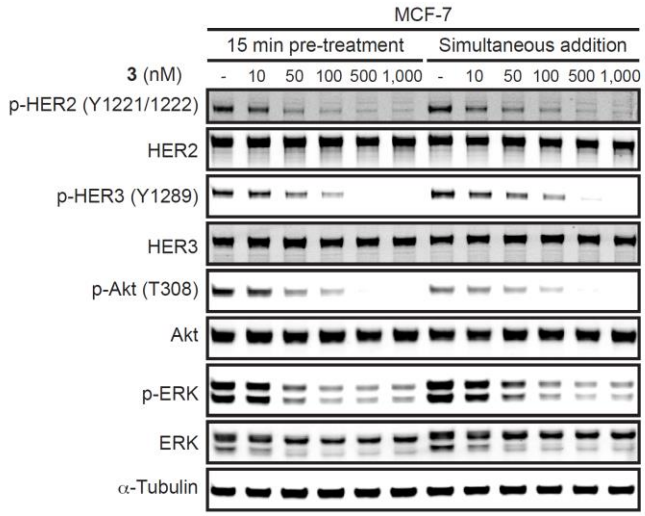

Figure 1.15. MCF-7 cells were serum starved for 24h and then either treated with **3** for 15 min followed by a 15 min NRG stimulation (50ng/mL) (15 min pre-treat), or **3** and NRG were added simultaneously for 15 min (simultaneous addition). **3** shows little to no shift in its ability to inhibit signaling +/- pre-incubation indicating it can bind to the actively signaling HER2/HER3 heterodimer.

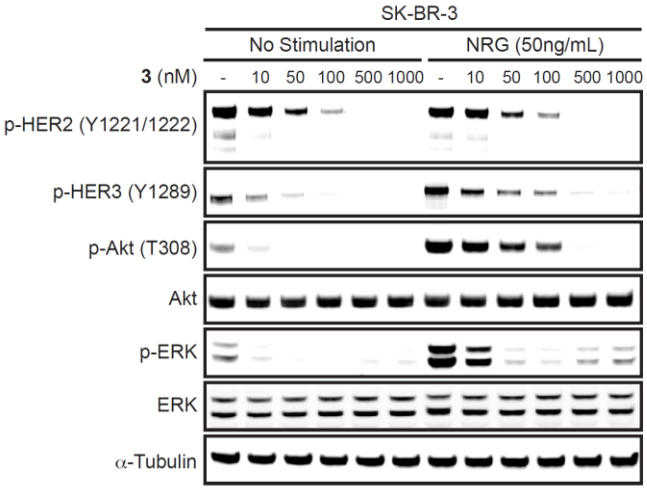

Figure 1.16. SK-BR-3 cells were serum starved for 24h and then either treated with NRG or vehicle for 15 min followed by varying concentrations of **3** for 15 min and signaling was analyzed by western blot.

Consistent with the results in the HER2-overexpressing cell lines, CW-2 cells were equally sensitive to **3** +/- NRG in both proliferation and signaling assays (Fig. 1.18a, b). This superior activity of **3** compared to lapatinib towards the CW-2 cells was not due solely to the

L755S mutation in HER2 as a similar trend was also seen in a Ba/F3 cell line dependent on the HER3 mutant, HER2YF/HER3E928G (2YF/3EG), which can grow independently of NRG (Fig. 1.17).

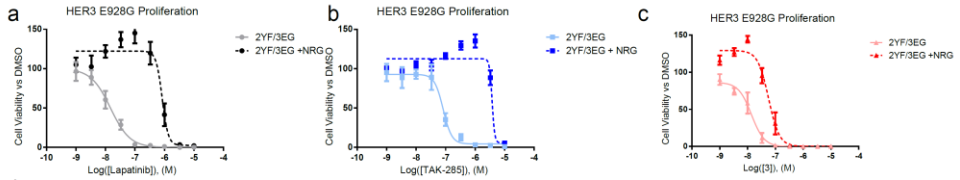

d

	2YF/3EG	2YF/3EG + NRG	NRG Fold Rescue
Lapatinib	15.7 ± 5.4	860.5 ± 99.6	55.0
TAK-285	97.7 ± 17.8	3,841.3 ± 319.7	39.3
3	14 ± 4.0	58 ± 13.5	4.1

Figure 1.17. NRG rescues HER3 mutant drive Ba/F3 cells. 48h proliferation of 2YF/HER3E928G (2YF/3EG) Ba/F3 cells treated with a dose response of **a**. lapatinib **b**. TAK-285 or **c**. **3** in the presence or absence of NRG. The large shift in the ability to inhibit proliferation by the current HER2 drugs shows that HER3 mutants could be rescued from the effects of HER2 drugs by NRG in a manner similar to HER2 over expressing cells (mean ± SD, n=3) **d**. Table of IC_{50} values for the 2YF/3EG cell lines (nM ± SD, n=3).

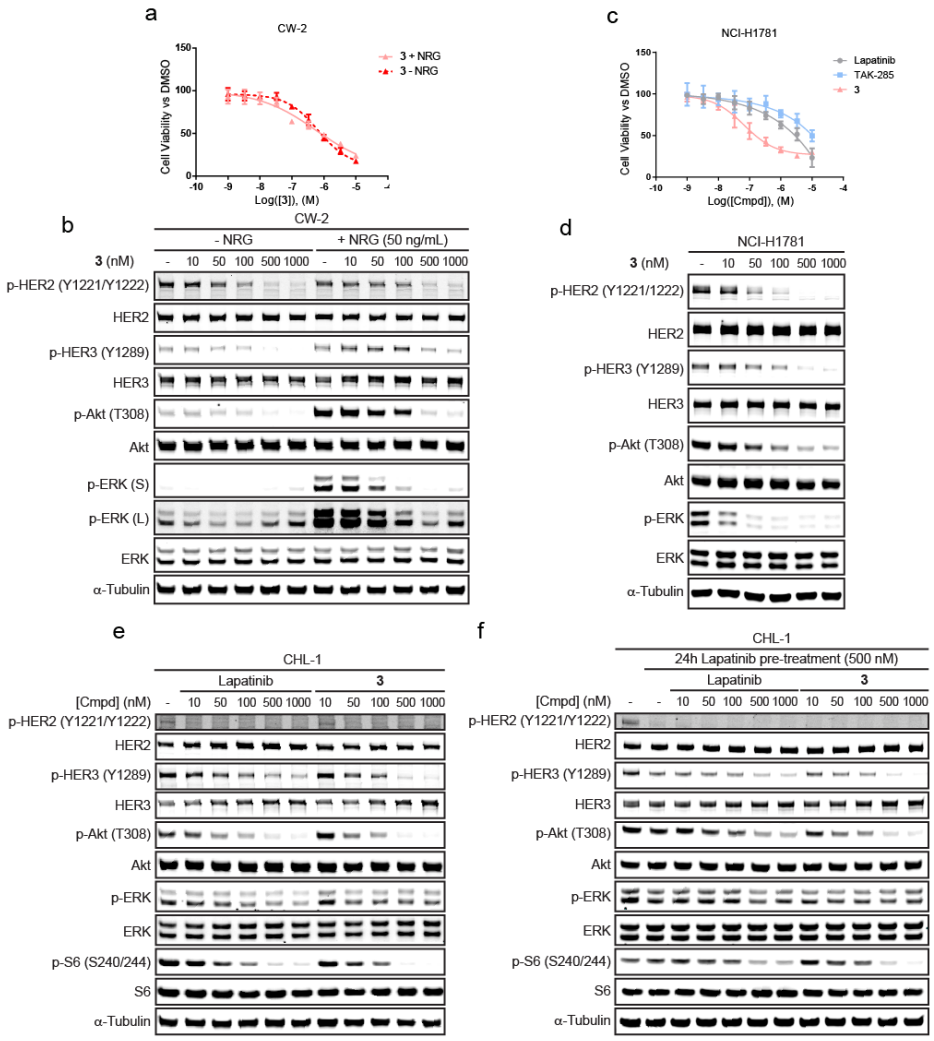

Figure 1.18. 3 inhibits the active HER2/HER3 heterodimer in multiple oncogenic settings. **a.** 72 h proliferation of CW-2 cells against **3** in the presence or absence of NRG (mean ± SD, n=3). **b.** CW-2 cells treated with a dose response of **3** in the presence or absence of NRG (50ng/mL) for 1h. **c.** 72 h proliferation of NCI-H1781 cells shows that they are sensitive to **3** but not to DFG in/α-C out inhibitors (mean ± SD, n=3). **d.** NCI-H1781 cells were treated with a dose response of **3** and signaling was evaluated after 15 min. **e.** HER2/HER3 signaling was evaluated in CHL-1 cells treated with a dose response of either lapatinib or **3** for 24 h. **3** is better able to inhibit p-HER3 and thus the PI3K/Akt pathway. **f.** CHL-1 cells were treated with either DMSO or 500 nM lapatinib for 24 h. The cells were then washed and treated with a dose response of either lapatinib or **3** for an additional 24 h. Signaling shows **3** is better able to inhibit feedback activated HER2/HER3 signaling in CHL-1 cells.

The ability of **3** to inhibit the activated form of HER2 was not limited to growth factor-induced heterodimers as the mutationally activated form of HER2 in NCI-H1781 cells was rapidly and fully inhibited by **3**, which translated into its ability to inhibit the proliferation of this cell line (Fig. 1.18c, d). To further evaluate the potential of **3** against HER2 mutants within a HER2/HER3 heterodimer, we transduced wt HER3 containing Ba/F3 cells with reported HER2 oncogenic mutants in the HER2YF construct[15,16]. The resulting cell lines contained the HER2 mutations L755S (2YF-L755S/3wt), Y772_A775 dup (2YF-YVMA/3wt), and G776del_insVC (2YF-VC/3wt) remained sensitive to **3** but showed complete resistance to lapatinib (Table 1.5).

Table 1.5. Table of IC_{50} values (nM ± S.D., n=3 for 2YF/3wt + IL-3, Axl, and 2YF/3wt + NRG. n=2 for 2YF-L755S/3wt + NRG, 2YF-YVMA/3wt + NRG, and 2YF-VC/3wt + NRG). NT = not tested.

	2YF/3wt + IL-3	Axl	2YF/3wt + NRG	2YF-L755S/3wt + NRG	2YF-YVMA/3wt + NRG	2YF-VC/3wt + NRG
Lapatinib	>3,333	>3,333	63.6 ± 12.5	>3,333	>10,000	>3,333
TAK-285	>10,000	>3,333	398.6 ± 110.7	NT	NT	NT
3	2,536.7 ± 217.2	1,172.3 ± 106.0	6.8 ± 0.2	38.2±2.9	11.4±0.1	7.7±1.0

An additional mechanism by which cancers can become dependent on HER2/HER3 dimers is through NRG mediated autocrine signaling[13]. Proliferation of the NRG autocrine dependent CHL-1 cell line was similar between lapatinib and **3** when measured at 72 h using CellTiter-Glo (Fig. 1.19a). However, monitoring the growth of CHL-1 cells using microscopy showed that the anti-proliferative activity of **3** is immediate and more potent when compared to

lapatinib, which takes some time to begin exerting its weaker anti-proliferative effect

(Supplementary Fig. 1.19b).

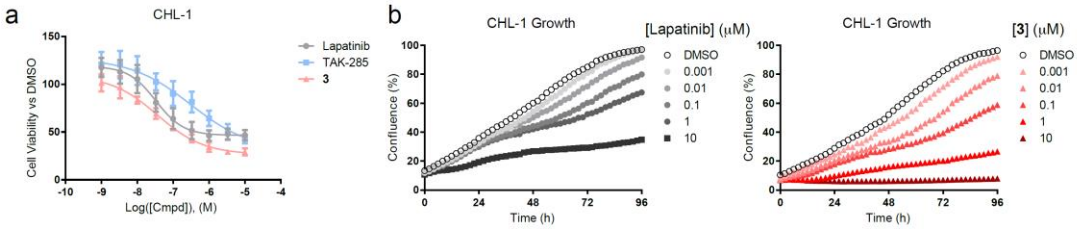

Figure 1.19. 3 is a more potent inhibitor of CHL-1 cell growth. **a**. 72h proliferation curves of CHL-1 cells treated with the indicated inhibitors (mean ± SD, n=3). **b**. The growth of CHL-1 cells treated with a dose response of either lapatinib (left) or **3** (right was monitored over 96h using the IncuCte Zoom (mean, n=2).

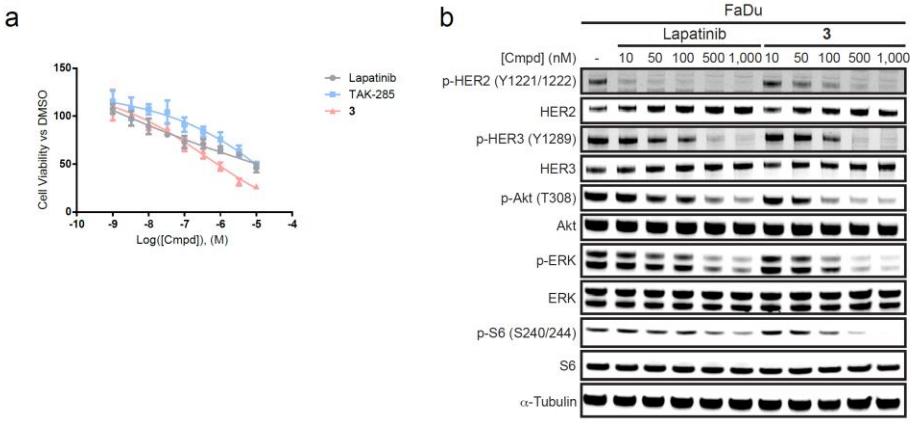

Figure 1.20. FaDu cells are more sensitive to **3** compared to lapatinib. **a.** 72h Proliferation of FaDu cells shows **3** is more effective than current HER2 inhibitors (mean ± SD, n=3). **b**. HER2/HER3 signaling was evaluated in FaDu cells treated with a dose response of either lapatinib or **3** for 24h. **3** is better able to inhibit pHER3 and its downstream signaling pathways.

We next examined signaling in CHL-1 cells after 24 h drug treatment and found that **3** was better able to inhibit NRG autocrine signaling in the presence of feedback, evidenced by the increasing expression of HER2 and HER3 with increasing concentration of drug (Fig. 1.18e). To further examine the differing abilities of **3** and lapatinib to inhibit feedback-released signaling in the NRG autocrine cells, we pre-treated CHL-1 cells with lapatinib for 24 h to induce feedback signaling, washed the cells, and then treated with a dose response of either lapatinib or **3** for an

additional 24 h. Whereas the ability of lapatinib to inhibit feedback signaling was reduced as compared to the 24 h treatment by itself, **3** showed little to no shift in its ability to inhibit signaling – and showed complete inhibition at 1 μM (Fig. 1.18f). Similar results were obtained in FaDu cells, which are also dependent on NRG autocrine signaling (Supplementary Fig. 1.20).

To determine the feasibility of using **3** *in vivo*, we analyzed the pharmacokinetics after either IV or IP administration in mice (Fig. 1.21). The short half-life of the inhibitor precluded a thorough test of **3** against xenografts and improving the PK properties of the inhibitor scaffold will be a focus of future optimization efforts.

a

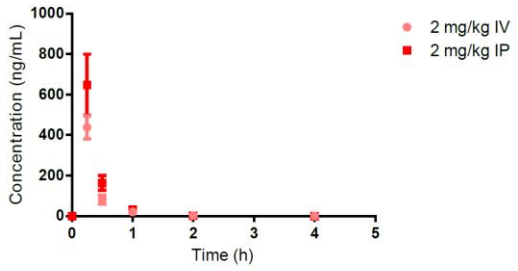

b

PK parameters of **3** in CD-1 mice following a single IV and IP dose

Administration Route	Dose (mg/kg)	Cmax (ng/mL)	Tmax (h)	AUC(0-24) (ng/mL*h)	T-HALF (h)	CL (L/h/kg)	Vd (L/Kg)	F%
IV	2	438	0.25	157	0.3	12.6	6.0	
IP	2	648	0.25	259	0.3	N/A	N/A	165%

Figure 1.21. Pharmacokinetics of **3**. **a**. Plasma concentration of **3** following a single administration of 2mg/kg by IV or IP. **b**. Pharmacokinetic parameters of **3**.

Discussion

The conformational dynamics of protein kinases are critical for their function and for many of the adaptable characteristics of kinase-driven signaling pathways. Particular kinase conformations also offer access to distinctive structural features that can be exploited in the design of inhibitors to gain selectivity even among well conserved protein families. The DFG in/α-C out binding inhibitor lapatinib targets the inactive state of a kinase with its benzyl ether

substituent, which when combined with the quinazoline scaffold grants it exquisite selectivity for the EGFR family of kinases. What has so far been largely unappreciated is the vulnerability of this class of inhibitors to mechanisms that stabilize the active state of the targeted kinases, which lead to drug resistance as we describe here.

Our study highlights this vulnerability and demonstrates that multiple mechanisms of stabilizing the active conformation of HER2 – through mutation or protein/protein interactions – results in resistance to lapatinib. The challenge is therefore to develop a potent inhibitor of the HER2/HER3 heterodimer whose selectivity is independent of binding to the inactive state. In order to discover such an inhibitor we turned to cell-based screening that has shown a unique ability to identify novel kinase inhibitors that target the relevant conformation of a protein in its endogenous environment[38,39]. A screen of close to one million small molecules revealed a novel inhibitor whose potency and selectivity were improved through iterative rounds of medicinal chemistry. The resulting EGFR family inhibitor demonstrates the striking ability to inhibit the mutationally activated form of HER2 as well as NRG-stabilized HER2/HER3 signaling complexes, both of which are insensitive to the clinical inhibitor lapatinib.

While our approach sought to find a single agent that could address the challenge of inhibiting the active HER2/HER3 heterodimer, alternative strategies using the HER2 targeting antibody pertuzumab in conjunction with T-DM1 have also been shown to be efficacious. This treatment regimen would require sufficient doses of both drugs to be consistently present for activity as either agent by itself is unable to inhibit signaling or growth of HER2 driven cells in the presence of NRG[20]. Additionally, this dual antibody-based strategy would be unable to target the p95 fragment of HER2, which is associated with trastuzumab resistance[40,41] and poorer clinical outcomes[42,43].

Another potential strategy to target the NRG-stimulated HER2/HER3 heterodimers is to use the irreversible inhibitor of HER2 neratinib. However, neratinib is based on the same DFG in/α-C out binding scaffold as lapatinib so while its electrophilic nature may make it more potent than lapatinib, it would also suffer from a reduced ability to initially bind to the activated form of HER2.

The last decade has seen an industrialization of kinase inhibitor discovery using purified protein kinases for both drug development and off-target assessment. In other target classes, such as GPCRs and ion channels, cell-based screens have been the rule rather than the exception and have led to a rich array of state specific modulators. Our work suggests that cell-based assays designed for kinases offer a powerful screening platform that can lead to a similar diversity in the state specificity of kinase inhibitors with the expectation that such state-specific binders will exhibit enhanced therapeutic benefit through potentially novel mechanisms of action.

Methods

Cell Culture and Reagents. BT-474, MCF-7, NCI-H1781, CHL-1, and FaDu cells were purchased from ATCC, CW-2 cells were purchased from Riken Cell Bank, HEK293T cells were purchased from the UCSF cell culture facility, and EcoPack-293 cells were purchased from Clontech. SK-BR-3 cells were a gift from Dr. Sourav Bandyopadhyay (UCSF) and parental Ba/F3 cells were a gift from Dr. Neil Shah (UCSF). All cell lines were maintained at 37°C and 5% CO_2. BT-474, NCI-H1781, CW-2, Axl+ Ba/F3, and 2YF/3EG Ba/F3 cells were maintained in RPMI-1640 (Gibco) + 10% FBS. MCF-7, CHL-1, FaDu, HEK293T, and EcoPack-293 cells were maintained in DMEM (Gibco) + 10% FBS. SK-BR-3 cells were maintained in McCoy's 5A (Gibco) + 10% FBS. Parental Ba/F3's were

maintained in RPMI-1640 + 10% FBS supplemented with 10 ng/mL IL-3. 2YF/3wt, 2YF/3TM, 2YFTM/3wt, 2YFTM/3TM, 2YF-L755S/3wt, 2YF-YVMA/3wt, and 2YF-VC/3wt Ba/F3 cells were maintained in RPMI-1640 + 10% FBS supplemented with 6.25 ng/mL NRG.

Lapatinib and TAK-285 were purchased from Selleckchem and were aliquoted and stored as 10mM DMSO stocks at -20°C. Anti-phospho-EGFR (Y1068) (cat#3777), anti-EGFR (cat#4267), anti-phospho-HER2 (Y1221/Y1222) (cat#2243), anti-HER2 (cat#2165), anti-phospho-HER3(Y1289) (cat#2842), anti-HER3 (cat#12708), anti-HER4 (cat#4795), anti-phospho-Akt(T308) (cat#2965), anti-Akt (cat#2920), anti-phospho-ERK (cat#9101), anti-ERK (cat#4695), anti-phospho-S6 (S240/244) (cat#2215), anti-S6 (cat#2217), anti-phospho-4-EBP1 (T37/46) (cat#2855), anti-4EBP1 (cat#9644), anti-α-tubulin (cat#3873), and human neuregulin-1 (cat#5218) were purchased from cell signaling technologies. Mouse IL-3 (cat#PMC0034) was purchased from Gibco.

Cloning and Ba/F3 Cell Selection. Site-directed mutagenesis was performed according to standard protocols on the human HER2 and HER3 sequences in pcDNA3.1. The desired constructs were Gibson cloned into the pMSCV plasmid (Clontech) containing the puro resistance (HER3, Axl) or neo resistance (HER2) gene[44]. The sequences of all constructs were confirmed with DNA sequencing. To produce virus, EcoPack-293 cells in a 6-well plate were transfected with the desired pMSCV plasmid using lipofectamine LTX (Invitrogen) according to the manufacturer's protocol. Media was exchanged 8h after transfection. 48 h after transfection the viral supernatant was filtered through a 0.2μM filter and added to one well of a 6 well plate containing $2x10^6$ Ba/F3 cells in 1 mL of RPMI media containing 40% FBS, 10 ng of IL-3, and 4 μg of polybrene (Sigma). The cells were then centrifuged at 2,000 x g for 90 min at room temperature, placed back in the incubator for 24 h, and then added to a T-75 flask containing

fresh RPMI-1640 media supplemented with 10 ng/mL of IL-3 and incubated for an additional 24h.

For the 2YF/3wt cells, the parental cells were first transduced with HER3 according to the protocol above and were then spun down at 500xg for 5 min and re-suspended in media supplemented with 10 ng/mL IL-3 and 3 μg/mL puromycin (Invitrogen). Cells were maintained in these conditions for seven days, passaging as required. After seven days the cells were spun down, washed with fresh media, and then used for a subsequent round of transduction according to the protocol above with HER2YF virus. 48h after the second transduction, the cells were re-suspended in RPMI-1640 containing 10 ng/mL IL-3 and 800 μg/mL G418 (Invitrogen). The cells were maintained in these conditions for seven days, passaging as required. After seven days the cells were spun down, washed with fresh media, and then suspended in media supplemented with 10 ng/mL of NRG. Cells were maintained in these conditions for seven days to select for a NRG dependent population of 2YF/3wt Ba/F3 cells that were then maintained as described above. The same protocol was used for the 2YF-L755S/3wt, 2YF-YVMA/3wt, and 2YF-VC/3wt cell lines using the indicated constructs.

For the HER2YF/3TM, HER2YFTM/3wt, and HER2YFTM/3TM Ba/F3 cell lines, an identical protocol was used with the exception that the populations were first selected for expression of the indicated HER2 construct (G418 resistance), followed by the expression of the indicated HER3 construct (puromycin resistance).

HER2YF/3EG Ba/F3 cells were selected according to the protocol for the HER2YF/3TM Ba/F3's with the exception that no NRG was supplemented in the media during IL-3 independent selection.

For Axl+ cells, the transduced cells were spun down at 500xg for 5 min and resuspended in media supplemented with 10 ng/mL IL-3 and 3 μg/mL puromycin (Invitrogen). Cells were maintained in these conditions for 7 days, passaging as required. After 7 days the cells were spun down, washed with fresh media, and then suspended in IL-3 free media. The cells were maintained in these conditions for 2 weeks to select for an IL-3 independent population of Axl+ driven cells.

Proliferation Assays. For adherent cell lines, cells were plated onto opaque white 96-well plates (Greiner cat#655083) and allowed to adhere overnight. The following day media was changed to fresh media that contained either DMSO or the indicated concentration of drug plus NRG (50ng/mL final concentration) as indicated. Plates were incubated at 37°C for 72h and cell viability was read out using CellTiter-Glo assay (Promega) according to the manufacturer's protocol. For Ba/F3 cell proliferation, cells, drug dilution, and any necessary growth factors (10 ng/mL IL-3 or 6.25 ng/mL NRG) were combined in a well of a 96 well plate. Plates were incubated at 37°C for 48h and proliferation was read out using CellTiter-Glo according to the manufacturer's protocol. For all normalized assays, proliferation was normalized to the DMSO control condition. All graphs were plotted in GraphPad Prism 6 and fit with a non-linear regression of the log(inhibitor) vs response with a variable slope where shown. All graphs are averages (+/- standard deviation) of biological triplicates each performed in technical triplicate unless otherwise noted.

Immunoblotting. Cells were grown in 6-well plates and treated according to the indicated conditions at which point the media was aspirated, cells were washed with 1 mL of cold PBS, which was then aspirated and the plates were frozen at -80°C. The frozen cells were thawed on the plates in a buffer containing 50mM Tris pH 7.5, 150mM NaCl, 1mM EDTA, and 1% Triton X-

100 supplemented with 1x phosphatase (PhoSTOP, Roche) and 1x protease (complete-mini tablets, Roche) inhibitors. Lysates were scraped, transferred to Eppendorf tubes, and cleared by centrifugation at 20,000xg for 20 min at 4°C. The clarified lysates were transferred to chilled, clean tubes, and normalized for protein concentration by Bradford (Bio-Rad). The normalized lysates were diluted with Laemmli loading buffer, and 10µg of total protein was run on a 4-12% gradient gel (Invitrogen), which was then transferred to .45 µM nitrocellulose (Bio-Rad) and analyzed using the indicated primary antibodies according to the manufacturer's recommendations (1:1000 antibody dilution). Primary antibodies were detected using IRDye secondary antibodies (Li-Cor) according to the manufacturer's recommendations and scanned on an Odyssey imager (Li-Cor). Scanned images were cropped and assembled in Adobe Illustrator 6.

For the HER3 immunoprecipitation cells were treated the same as above but lysed in a buffer containing 20 mM Tris pH=7.5, 150mM NaCl, 1mM EDTA, and 1% Triton X-100 supplemented with 1x phosphatase (PhoSTOP, Roche) and 1x protease (complete-mini tablets, Roche) inhibitors. 1 mg of of the total protein was immunoprecipitated with the HER3 anti-body (CST, cat#12708) at 4°C overnight, followed by incubation with protein A beads (CST cat#8687) for 30 min at room temperature. The beads were washed 3x with lysis buffer, eluted by boiling in 3x laemmli buffer and analyzed by western blot as detailed above.

High Throughput Screening and Analysis. This work was conducted by Sirkku Pollari and Weijun Shen at the California Institute for Biomedical Research (CALIBR). For compound screening, 20 nL of 1 mM compound solutions in DMSO were transferred (Echo Labcyte) into white 1,536-well plates. Subsequently, cells were seeded in 5 µL of growth medium (500 cells per well) using an automated plate filler (Kalypsys), resulting in 4 µM compound concentration. Each assay

plate included neutral (DMSO only) and inhibitor (lapatinib) control wells. CellTiter-Glo Reagent (Promega, 2 µL/well) was added two days later. Luminescence signal was read after 10 minutes using an automated plate reader (ViewLux or Envision, Perkin-Elmer). The data were analyzed using the Genedata Screener software, normalized by neutral control. The percentage inhibition for each tested compound was calculated on per-plate basis, and all compounds that showed over 50% inhibition of the luminescence signal as compared to the DMSO control were picked as primary hits for triplicate confirmation. Hits confirmed with > 50% inhibition in two out of the three replicates were subsequently assayed in parental Ba/F3 +IL3 cells and non-toxic hits (< 30% inhibition in parental cells) were further assayed in dose response in 2YF/3wt + NRG, parental BaF3 +IL-3, and BaF3-Axl cells in order to identify hits that selectively inhibit the 2YF/3wt cells in the presence of NRG.

***In vitro* Kinome Screen.** *In vitro* profiling of **2** at 100 nM and 1 µM and **3** at 1 µM was conducted by Nanosyn.

Real-Time Cell Proliferation Assay. CHL-1 cells were plated in clear bottom black 96-well plates (Corning cat# 3904) and allowed to adhere overnight. The following day media was changed to fresh media that contained either DMSO or the indicated concentration of compound. Confluence was measured every 2 h for 96 h using two bright field images per well taken on an IncuCyte Zoom (Essen BioScience). Data were graphed in GraphPad Prism 6 and are averages of biological duplicates, each performed in technical triplicate.

***In vitro* HER2 Kinase Assay.** *In vitro* kinase assays with the HER2 kinase domain (SignalChem) were performed in triplicate as follows. To 9 µL of a 2.5x solution of kinase and substrate in reaction buffer was added 3µL of a 5x DMSO or inhibitor dilution in 10% DMSO:water. The inhibitor/kinase solution was incubated at room temperature for 10 minutes. The kinase assay

was initiated by the addition of 3 µL of a 5x solution of ATP, and ran for 15 minutes. The final reaction conditions were 50mM Tris (pH7.4), 5mM $MnCl_2$, 0.01% Tween-20, 2mM DTT, 100 µM E_4Y substrate (SignalChem), 15 nM HER2, 2% DMSO, 50 µM ATP, and 1 µCi γ^{32}P-ATP. After 15 minutes, 3 µL of each reaction was pipetted onto phosphocellulose sheets (P81, Whatman) and allowed to dry. The sheets were then washed 4 x 5 min with a solution of 0.5% phosphoric acid, dried, and exposed to a phosphor screen overnight. Phosphorimaging was conducted on a Typhoon 9500, image intensities were quantified in ImageQuant 5.2, normalized to the DMSO control and plotted in GraphPad Prism 6.

HER3 Thermofluor Assay. The HER3 gatekeeper mutation (T787M) was introduced into the HER3 tyrosine kinase domain in the pFastBac plasmid using standard protocols. Both wt and T787M HER3 were purified according to the previously published protocols[35]. Thermofluor reactions were performed in duplicate and set up as follows. 1 µL of an inhibitor or DMSO dilution in 40% DMSO:water was added to 19 µL of the HER3 kinase domain in reaction buffer. The final reaction solution contained 100 mM MOPS, 200 mM NaCl, 5% glycerol, 5 mM MgCl2, 0.1 mM DTT, 5x SYPRO Orange, 2 µM kinase, 2% DMSO and 20 µM inhibitor in the wells of a 96-well, low profile, white, PCR plate (USA scientific). The solution was pipetted up and down to mix, sealed with TempAssure clear PCR flat caps (USA Scientific), centrifuged at 500xg for 30 s, and heated in a Stratagene Mx3005P RT-PCR machine from 25°C to 95°C in 0.5°C increments every 30 s after an initial incubation at 25°C for 10 min. Fluorescence was measured at the end of each 30s period with an excitation wavelength of 492 nm and an emission wavelength of 610 nm. To obtain the melting temperature, fluorescent signals were normalized to the maximum fluorescent signal for that well. Values after the well had reached a maximum signal were discarded and the signals were fit to the Boltzmann equation in Graphpad Prism 6. ΔT_m was

calculated as the difference in melting temperature between the compound-treated kinase compared to the DMSO control.

Transfected HER2 Kinase Activity. The HER2 gatekeeper mutation (T798M) was introduced into the HER2 gene in pcDNA3.1 using standard protocols. HEK293T cells were transfected with the indicated pcDNA3.1 constructs of HER2 using Lipofectamine LTX according to the manufacturers protocol. 24h after transfection the media was exchanged for fresh drug containing media. After 1h of drug treatment the cells were processed for immunoblots according to the above protocol.

Cell Death Assay. Cells were plated in clear bottom, black, 96-well plates (Corning cat#3904) and allowed to adhere overnight. The following day media was changed to fresh media that contained 1x concentration of CellTox green (Promega) and either DMSO or the indicated concentration of drug +/- NRG (50ng/mL). Cells were allowed to grow for 72 h after which the number of dead cells was measured using the IncuCyte Zoom. Immediately after the 72 h read, 5 µL of 1.25% Triton X-100 was added to each well, which were then incubated at 37°C for 30 min to lyse all cells that were then counted by the IncuCyte. The percent cell death was calculated by dividing the number of dead cells counted at 72h by the number of total DNA containing cells after the detergent treatment. Values are the average of biological triplicate each performed in technical triplicate and were plotted in GraphPad Prism 6.

Crystallization and Structure Determination. This work was conducted by Jin Park and Mark Lemmon at the University of Pennsylvania. $EGFR^{672-998}$/V924R protein expression and purification was performed exactly as previously described[34]. For the EGFR TKD^{V924R}/**2** structure, EGFR TKD protein was concentrated to 8 mg/ml in 20 mM Tris-HCl, pH 8.0, containing 150 mM NaCl and 2 mM DTT. Protein was co-crystallized with excess of a drug **2** (1:2 molar ratio) in a

reservoir solution of 1.34M ammonium sulfate, 1.34% (v/v) PEG 400, and 0.1 M sodium acetate/acetic acid pH 5.5 in the hanging drop at 21˚C. Crystals were cryo-protected in reservoir solution with added 20% (w/v) glycerol and flash frozen in liquid nitrogen. Diffraction data were collected at beamline 23ID-B of GM/CA@APS (Advanced Photon Source), where crystals diffracted to 3.3 Å, and were processed using HKL2000 (see Supplementary Table 2). The structure was solved by molecular replacement using Phaser with the active EGFR (WT) TKD structure (PDB 1M17) as an initial search model. Repeated cycles of manual building/rebuilding using Coot were alternated with rounds of refinement employing REFMAC and PHENIX, plus composite omit maps calculated using PHENIX. Coordinates, parameter files and molecular topology of **2** were generated by PRODRG[45]. Structural figures were generated with PyMOL.

Pharmacokinetic Evaluation of 3. Pharmacokinetic profiling of compound **3** was performed by Biotranex.

Accession Codes. The macromolecular structure has been deposited with Protein Data Bank under the accession number 5JEB.

Chemical Synthesis

General Methods: Reactions were performed in sealed vials with magnetic stirring. All commercial reagents were used without further purification. All microwave reactions were performed on a discover system (CEM). Silica gel chromatography was performed on a Combiflash Rf + using column cartridges pre-packed with 40-60 micron silica (Teledyne Isco). All RP-HPLC were performed with a Waters 2545 binary gradient module equipped with an XBridge prep C18 column using H2O + 0.1% formic acid and CH3CN + 0.1% formic acid (5-95% gradient) while monitoring at 254 nm. Low resolution mass spectra (LC/ESI-MS) were recorded in positive and negative mode on a Waters TQ detector with an Acquity UPLC equipped with a BEH C18

column. ^{1}H and ^{13}C NMR spectra were recorded on a Bruker Avance III HD 400 spectrometer or a Bruker Avance DRX500 spectrometer and referenced to solvent peaks. Coupling constants (*J*) are reported in hertz, chemical shifts are reported in δ (ppm) as either s (singlet), d (doublet), t (triplet), dd (doublet of doublets), dt (doublet of triplets), or m (multiplet).

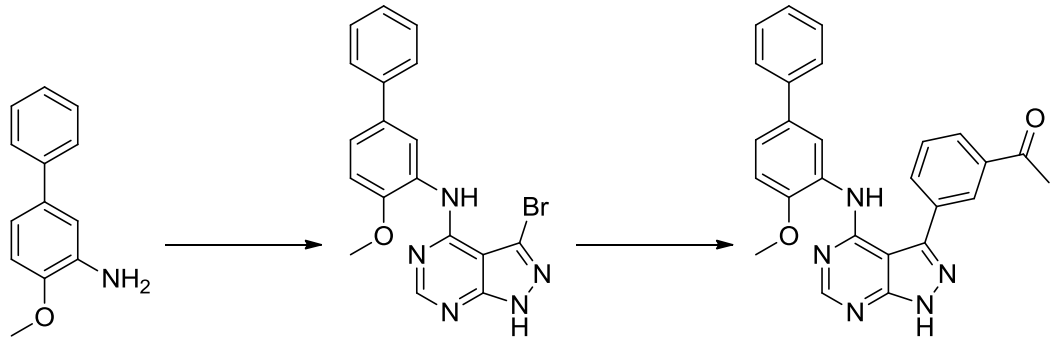

1-(3-(4-((4-methoxy-[1,1'-biphenyl]-3-yl)amino)-1H-pyrazolo[3,4-d]pyrimidin-3-yl)phenyl)ethanone (**1**): A microwave tube containing 19.3 mg of 5-phenyl-o-anisidine (0.097 mmol), 25.1 mg of 3-bromo-4-chloro-1H-pyrazolo[3,4-d]pyrimidine (0.11 mmol), 9.2 µL of glacial acetic acid (0.16 mmol) and 1 mL of n-butanol with a stir bar was capped and heated to 130°C for 15 min in a microwave reactor. The reaction was cooled and concentrated by rotary evaporation. The residue was recrystallized in ethanol to give 30.7 mg of crude **4** as a white solid. The crude **4** was added to a microwave tube containing 54.2 mg of 3-acetylphenyl-boronic acid (0.31 mmol), and 68.5 mg of potassium phosphate (0.31 mmol) in 1.5 mL of dioxane:H_2O (3:1) with a stir bar, which was sparged with argon for 5 min. 6.3 mg of XPhos Pd G2 (.0078 mmol) and 7.8 mg of SPhos (.016 mmol) were then added to the microwave tube which was purged with argon and heated to 150°C for 20 min in a microwave. The reaction was cooled, concentrated *in vacuo*, and the residue was purified by silica gel chromatography (eluent,

Hex:EtOAc = 3:1 to 1:3) to give 26.4 mg (62.5% over 2 steps) of **1** as a white powder. MS (ES+) *m/z* 436.9 $(M + H)^{+1}$; ^{1}H NMR (DMSO-d_6, 400 MHz) δ 1.66 (s, 3H), 3.60 (s, 3H), 7.08 (d, 1H, *J*=8.6 Hz), 7.33 (m, 2H), 7.47 (t, 2H, *J* =7.7 Hz), 7.62 (m, 2H), 7,84 (t, 1H, *J*=7.7 Hz), 7.98 (s, 1H), 8.06 (dt, 1H, *J*=7.7, 1.3 Hz), 8.21 (dt, 1H, *J*=7.8, 1.3 Hz), 8.33 (t, 1H, *J*=1.5 Hz), 8.60 (s, 1H), 9.12 (d, 1H, *J*=2.2 Hz), 14.04 (s, 1H) ; ^{13}C NMR(DMSO-d6, 400 MHz) δ 27.29, 56.19, 99.25, 111.45, 118.68, 121.87, 126.84, 127.38, 128.70, 128.86, 129.08, 129.40, 130.35, 133.3, 133.73, 133.97, 137.98, 140.71, 143.5, 148.09, 154.45, 155.99, 156.1, 198.1.

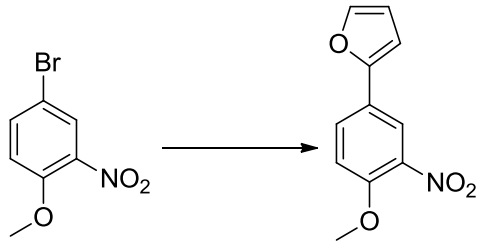

5

2-(4-methoxy-3-nitrophenyl)furan (**5**): A vial containing a stir bar and a solution of 166.3mg of 4-bromo-2-nitroanisole (.72 mmol) and 247.6 mg 2-Furanylboronic acid MIDA ester (1.11 mmol) in 4.35 mL of 1,2 dimethoxyethane and 2.9 mL of 1M Na_2CO_3 in H_2O was sparged with argon for 5 min. 172 mg of Tetrakis(triphenylphosphine)palladium(0) (0.15 mmol) was added and the reaction, which was purged with argon and stirred at 80°C for 12h. The reaction was cooled and water was added to the reaction mixture, which was extracted 3 times with dichloromethane. The combined organic layer was washed with brine, dried with anhydrous sodium sulfate, filtered and concentrated by rotary evaporation. The residue was purified by silica gel chromatography (eluent, Hex:EtOAc = 1:0 to 3:1) to give 140.4 mg (89%) of **5** as a yellow solid. MS (ES+) *m/z* 220.4 $(M + H)^{+1}$; ^{1}H NMR (DMSO-d_6, 400 MHz) δ 3.96, (s, 3H), 6.62 (dd, 1H, *J*=3.4,

1.8 Hz). 7.03 (dd, 1H, *J*=3.4, 0.7 Hz), 7.44 (d, 1H, *J*=9.1 Hz), 7.77 (dd, 1H, *J*=1.8, 0.7 Hz), 7.97 (dd, 1H, *J*=8.8, 2.3 Hz), 8.17 (d, 1H, *J*=2.3 Hz); ^{13}C NMR(DMSO-d6, 500 MHz) δ 57.31, 106.85, 112.74, 115.50, 120.06, 123.67, 129.43, 140.11, 143.72, 151.28, 151.37.

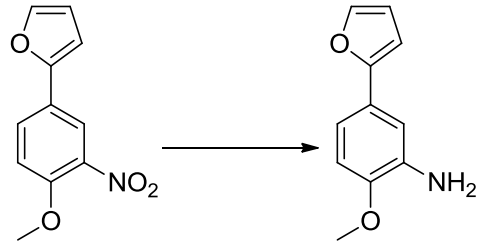

5 **6**

5-(furan-2-yl)-2-methoxyaniline (**6**): To a vial containing a stir bar and 131.4 mg of **5** (0.6 mmol) in 2 mL THF was added 686 µL glacial acetic acid (12 mmol). The solution was stirred at 0°C for 5 min and 1.178 g of powdered zinc (18 mmol) was added. The reaction was allowed to warm to room temperature over 1h. The reaction was then diluted with MeOH, filtered, and concentrated *in vacuo*. The resulting residue was extracted from saturated sodium bicarbonate with 3 portions of dichloromethane. The pooled organic layer was dried with anhydrous sodium sulfate, filtered, and concentrated to give 94.4 mg (83%) of **6** as an off white solid. MS (ES+) *m/z* 190.6 $(M + H)^{+1}$; ^{1}H NMR (DMSO-d_6, 400 MHz) δ 3.79 (s, 3H), 4.82 (s, 2H), 6.51 (dd, 1H, *J*= 3.3, 1.8 Hz), 6.6 (dd, 1H, *J*=3.3, 0.7 Hz), 6.83 (d, 1H, *J*=8.5 Hz), 6.9 (dd, 1H, *J*=8.3, 2.1 Hz), 6.99 (d, 1H, *J*=2.07 Hz), 7.63 (dd, 1H, 1.7, 0.7 Hz); ^{13}C NMR(DMSO-d6, 400 MHz) δ 55.82, 103.8, 109.44, 111.17, 112.22, 112.42, 123.95, 138.32, 142.08, 146.58, 154.45.

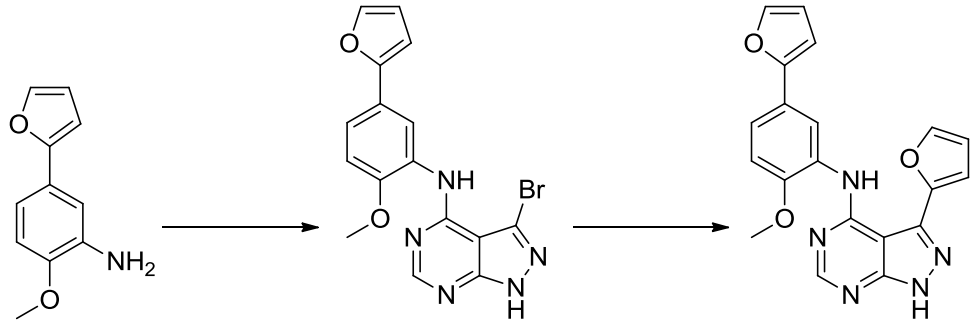

3-(furan-2-yl)-N-(5-(furan-2-yl)-2-methoxyphenyl)-1H-pyrazolo[3,4-d]pyrimidin-4-amine (**2**): **2** was obtained in 66% yield over 2 steps as a white powder by a method similar to the one described for compound **1**. MS (ES+) *m/z* 374.2 $(M + H)^{+1}$; ^{1}H NMR (DMSO-d_6, 400 MHz) δ 4.02 (s, 3H), 6.60 (dd, 1H, *J*=3.3, 1.8Hz), 6.81 (dd, 1H, *J*=3.3, 0.7 Hz), 6.83 (dd, 1H, *J*=3.4, 1.8 Hz), 7.09 (dd, 1H, *J*=3.5, 0.7 Hz), 7.21 (d, 1H, *J*=8.7Hz), 7.45 (dd, 1H, *J*=8.5, 2.1Hz), 7.75 (dd, 1H, *J*=1.7, 0.6Hz), 8.02 (dd, 1H, *J*=1.8, 0.7Hz), 8.57 (s, 1H), 9.25 (d, 1H, *J*=2.2Hz), 9.64 (s, 1H), 14.05 (s, 1H); ^{13}C NMR(DMSO-d6, 400 MHz) δ 56.97, 97.96, 104.93, 108.49, 111.7, 112.45, 113.15, 116.44, 119.34, 123.71, 128.84, 142.76, 143.88, 147.91, 148.54, 153.77, 154.03, 155.92, 156.15.

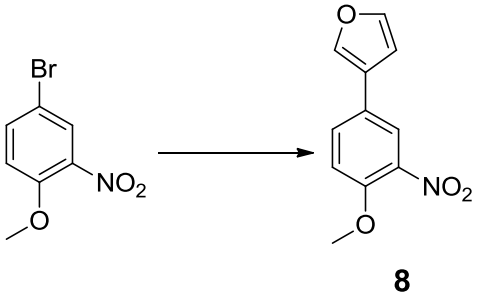

3-(4-methoxy-3-nitrophenyl)furan (**8**): **8** was obtained in 90% yield as a yellow solid by a method similar to the one described for compound **5**. MS (ES+) *m/z* 220.4 $(M + H)^{+1}$; ^{1}H NMR (DMSO-d_6, 400 MHz) δ 3.95 (s, 3H), 7.04 (dd, 1H, *J*=1.9,0.9), 7.39 (d, 1H, *J*=8.8), 7.76 (t, 1H, *J*=1.7), 7.91 (dd, 1H, *J*=8.7, 2.4), 8.12 (d, 1H, *J*=2.4Hz), 8.27 (m, 1H); ^{13}C NMR(DMSO-d6, 500 MHz) δ 57.23, 109.05, 115.23, 121.8, 124.26, 125.26, 131.50, 140.17, 145.00, 150.94.

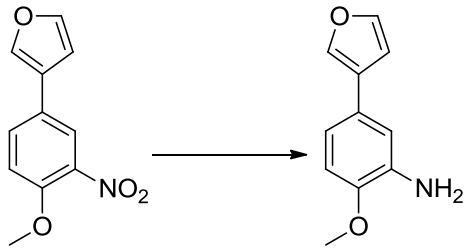

8 **9**

5-(furan-3-yl)-2-methoxyaniline (**9**): **9** was obtained in 92% yield as a pale yellow solid by a method similar to the one described for compound **6**. MS (ES+) *m/z* 190.7 $(M + H)^{+1}$; ^{1}H NMR (DMSO-d_6, 400 MHz) δ 3.77 (s, 3H), 4.71 (s, 2H), 6.75 (m, 1H), 6.77 (d, 1H, 2.10), 6.80 (d, 1H, 8.35 Hz), 6.85 (d, 1H, *J*=2.0Hz), 7.67 (t, 1H, *J*=1.7Hz), 7.90 (m, 1H); ^{13}C NMR(DMSO-d6, 400 MHz) δ 58.82, 109.26, 111.27, 111.60, 114.23, 125.06, 126.74, 138.20, 138.24, 144.28, 146.18.

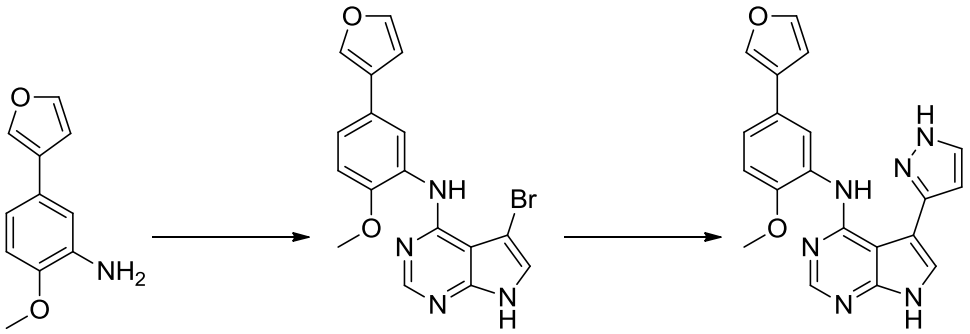

N-(5-(furan-3-yl)-2-methoxyphenyl)-5-(1H-pyrazol-3-yl)-7H-pyrrolo[2,3-d]pyrimidin-4-amine (**3**): A microwave vial containing 45.0 mg of **9** (0.24 mmol), 62.7 mg of 7-Bromo-6-chloro-7-deazapurine (0.27 mmol), 22.2 µL of glacial acetic acid (0.39 mmol) and 2.5 mL of n-butanol with a stir bar was capped and heated to 130°C for 17 min in a microwave reactor. The reaction was cooled and concentrated by rotary evaporation. The residue was recrystallized in ethanol to give 35.5 mg of crude **10** as a brown solid. The crude **10** was added to a microwave tube containing 70.2 mg of 1H-Pyrazole-5-boronic acid pinacol ester (0.36 mmol), and 81 mg of potassium phosphate (0.38 mmol) in 1 mL of dioxane:H_2O (3:1) with a stir bar, which was sparged with argon for 5 min. 7.5 mg of XPhos Pd G2 (.0097 mmol) and 7.3 mg of SPhos (0.018 mmol) were then added to the microwave tube which was purged with argon and heated to 150°C for 20 min in a microwave. The reaction was cooled and run on RP-HPLC. The product containing fractions were concentrated *in vacuo*, and the residue was purified by silica gel chromatography (eluent, Hex:EtOAc = 3:1 to 0:1) to give 12.4 mg (15% over 2 steps) of **3** as an off white powder. MS (ES-) *m/z* 371.6 $(M - H)^{-1}$; ^{1}H NMR (DMSO-d_6, 400 MHz) δ 3.92 (s, 3H), 6.72 (d, 1H, *J*=2.2), 6.87 (dd, 1H, *J*=1.8, 0.8 Hz), 7.08 (d, 1H, *J*=8.60 Hz), 7.27 (dd, 1H, *J*=8.3, 2.2Hz), 7.73 (m, 2H), 7.83 (d, 1H, *J*=2.3Hz), 8.04 (m, 1H), 8.28 (s, 1H), 8.78 (d, 1H, *J*=2.2Hz), 11.67 (s, 1H), 11.93 (s, 1H), 12.79

(s, 1H);); ^{13}C NMR(DMSO-d6, 400 MHz) δ56.63, 101.33, 101.94, 109.20, 109.40, 111.79, 120.34, 120.62, 121.11, 124.46, 126.60, 130.01, 130.65, 138.67, 144.51, 146.87, 149.99, 151.86, 152.14, 154.94.

References

1. Lemmon, M. A. *et al.* The EGFR Family: Not So Prototypical Receptor Tyrosine Kinases. *Cold Spring Harbor Perspectives in Biology* **6,** a020768–a020768 (2014).
2. Kovacs, E., Zorn, J. A., Huang, Y., Barros, T. & Kuriyan, J. A Structural Perspective on the Regulation of the Epidermal Growth Factor Receptor. *Annu Rev Biochem* **84,** 739–764 (2015).
3. Doerner, A., Scheck, R. & Schepartz, A. Growth Factor Identity Is Encoded by Discrete Coiled-Coil Rotamers in the EGFR Juxtamembrane Region. *Chem Biol* **22,** 776–784 (2015).
4. Zhang, X., Gureasko, J., Shen, K., Cole, P. A. & Kuriyan, J. An Allosteric Mechanism for Activation of the Kinase Domain of Epidermal Growth Factor Receptor. *Cell* **125,** 1137–1149 (2006).
5. Schneider, M. R. & Yarden, Y. The EGFR-HER2 module: a stem cell approach to understanding a prime target and driver of solid tumors. *Oncogene* (2015). doi:10.1038/onc.2015.372
6. Yarden, Y. & Sliwkowski, M. X. Untangling the ErbB signalling network. *Nat Rev Mol Cell Biol* **2,** 127–137 (2001).
7. Brewer, M. R. *et al.* Mechanism for activation of mutated epidermal growth factor receptors in lung cancer. *Proc Natl Acad Sci USA* **110,** E3595-E3604 (2013).
8. Wang, Z. *et al.* Mechanistic insights into the activation of oncogenic forms of EGF

receptor. *Nat Struct Mol Biol* **18,** 1388–1393 (2011).

9. Foster, S. A. *et al.* Activation Mechanism of Oncogenic Deletion Mutations in BRAF, EGFR, and HER2. *Cancer Cell* **29**, 477-493 (2016).

10. Lee-Hoeflich, S. T. *et al.* A Central Role for HER3 in HER2-Amplified Breast Cancer: Implications for Targeted Therapy. *Cancer Res* **68,** 5878–5887 (2008).

11. Tzahar, E. *et al.* A hierarchical network of interreceptor interactions determines signal transduction by Neu differentiation factor/neuregulin and epidermal growth factor. *Mol. Cell. Biol.* **16,** 5276–5287 (1996).

12. Vaught, D.B. *et al.* HER3 Is Required for HER2-Induced Preneoplastic Changes to the Breast Epithelium and Tumor Formation. *Cancer Res* **72,** 2672–2682 (2012).

13. Jaiswal, B. S. *et al.* Oncogenic ERBB3 Mutations in Human Cancers. *Cancer Cell* **23,** 603–617 (2013).

14. Wilson, T.R. *et al.*. Neuregulin-1-Mediated Autocrine Signaling Underlies Sensitivity to HER2 Kinase Inhibitors in a Subset of Human Cancers. *Cancer Cell* **20,** 158–172 (2011).

15. Bose, R. *et al.* Activating HER2 Mutations in HER2 Gene Amplification Negative Breast Cancer. *Cancer Discovery* **3,** 224 (2012).

16. Wang, S. E. *et al.* HER2 kinase domain mutation results in constitutive phosphorylation and activation of HER2 and EGFR and resistance to EGFR tyrosine kinase inhibitors. *Cancer Cell* **10,** 25–38 (2006).

17. Greulich, H. *et al.* Functional analysis of receptor tyrosine kinase mutations in lung cancer identifies oncogenic extracellular domain mutations of ERBB2. *Proc Natl Acad Sci USA* **109,** 14476–14481 (2012).

18. Geyer, C. E. *et al.* Lapatinib plus Capecitabine for HER2-Positive Advanced Breast Cancer.

N Engl J Med **355,** 2733–2743 (2006).

19. Verma, S. *et al.* Trastuzumab Emtansine for HER2-Positive Advanced Breast Cancer. *N Engl J Med* **367,** 1783–1791 (2012).

20. Phillips, G.D. *et al.* Dual Targeting of HER2-Positive Cancer with Trastuzumab Emtansine and Pertuzumab: Critical Role for Neuregulin Blockade in Antitumor Response to Combination Therapy. *Clin Cancer Res* **20,** 456 (2013).

21. Wilson, T. R. *et al.* Widespread potential for growth-factor-driven resistance to anticancer kinase inhibitors. *Nature* **487,** 505–509 (2012).

22. Sergina, N. V. *et al.* Escape from HER-family tyrosine kinase inhibitor therapy by the kinase-inactive HER3. *Nature* **445,** 437 (2007).

23. Chakrabarty, A., Sanchez, V., Kuba, M. G., Rinehart, C. & Arteaga, C. L. Feedback upregulation of HER3 (ErbB3) expression and activity attenuates antitumor effect of PI3K inhibitors. *Proc Nat Acad Sci USA* **109,** 2718 (2011).

24. Chandarlapaty, S. *et al.* AKT Inhibition Relieves Feedback Suppression of Receptor Tyrosine Kinase Expression and Activity. *Cancer Cell* **19,** 58–71 (2011).

25. Amin, D. N. *et al.* Resiliency and vulnerability in the HER2-HER3 tumorigenic driver. *Sci Transl Med* **2,** 16ra7 (2010).

26. Das, P. M. *et al.* Reactivation of epigenetically silenced HER4/ERBB4 results in apoptosis of breast tumor cells. *Oncogene* **29,** 5214–5219 (2010).

27. Sartor, C. I. *et al.* HER4 Mediates Ligand-Dependent Antiproliferative and Differentiation Responses in Human Breast Cancer Cells. *Mol Cell Biol* **21,** 4265-4275 (2001).

28. Aertgeerts, K. *et al.* Structural Analysis of the Mechanism of Inhibition and Allosteric Activation of the Kinase Domain of HER2 Protein. *J Biol Chem* **286,** 18756–18765 (2011).

29. Wood, E. R. *et al.* A unique structure for epidermal growth factor receptor bound to GW572016 (Lapatinib): relationships among protein conformation, inhibitor off-rate, and receptor activity in tumor cells. *Cancer Res* **64,** 6652–6659 (2004).

30. Littlefield, P. *et al.* Structural analysis of the EGFR/HER3 heterodimer reveals the molecular basis for activating HER3 mutations. *Sci Signal* **7,** ra114 (2014).

31. Brewer, M. R. *et al.* The Juxtamembrane Region of the EGF Receptor Functions as an Activation Domain. *Mol Cell* **34,** 641 (2009).

32. Warmuth, M., Kim, S., Gu, X.-J., Xia, G. & Adrian, F. Ba/F3 cells and their use in kinase drug discovery. *Curr Opin Oncol* **19,** 55–60 (2006).

33. Jura, N. *et al.* Mechanism for Activation of the EGF Receptor Catalytic Domain by the Juxtamembrane Segment. *Cell* **137,** 1293–1307 (2009).

34. Park, J. H., Liu, Y., Lemmon, M. A. & Radhakrishnan, R. Erlotinib binds both inactive and active conformations of the EGFR tyrosine kinase domain. *Biochem J* **448,** 417–423 (2012).

35. Shi, F., Telesco, S. E., Liu, Y., Radhakrishnan, R. & Lemmon, M. A. ErbB3/HER3 intracellular domain is competent to bind ATP and catalyze autophosphorylation. *Proc Natl Acad Sci USA* **107,** 7692–7697 (2010).

36. Jura, N. *et al.* Structural analysis of the catalytically inactive kinase domain of the human EGF receptor 3. *Proc Natl Acad Sci USA* **106,** 21608–21613 (2009).

37. Rexer, B. N. *et al.* Human Breast Cancer Cells Harboring a Gatekeeper T798M Mutation in HER2 Overexpress EGFR Ligands and Are Sensitive to Dual Inhibition of EGFR and HER2. *Clin Cancer Res* **19,** 5390–5401 (2013).

38. Yoshida, T. *et al.* Identification and characterization of a novel chemotype MEK inhibitor

able to alter the phosphorylation state of MEK1/2. *Oncotarget* **3**, 1533-1545 (2012).

39. Adrián, F. J. *et al.* Allosteric inhibitors of Bcr-abl-dependent cell proliferation. *Nature Chemical Biology* **2,** 95–102 (2006).

40. Scaltriti, M. *et al.* Expression of p95HER2, a truncated form of the HER2 receptor, and response to anti-HER2 therapies in breast cancer. *J Natl Cancer Inst* **99,** 628–638 (2007).

41. Chandarlapaty, S. *et al.* Inhibitors of HSP90 block p95-HER2 signaling in Trastuzumab-resistant tumors and suppress their growth. *Oncogene* **29,** 325–334 (2009).

42. Sperinde, J. *et al.* Quantitation of p95HER2 in paraffin sections by using a p95-specific antibody and correlation with outcome in a cohort of trastuzumab-treated breast cancer patients. *Clin Cancer Res* **16,** 4226–4235 (2010).

43. Sáez, R. *et al.* p95HER-2 predicts worse outcome in patients with HER-2-positive breast cancer. *Clin Cancer Res* **12,** 424–431 (2006).

44. Gibson, D. G. *et al.* Enzymatic assembly of DNA molecules up to several hundred kilobases. *Nat Meth* **6,** 343–345 (2009).

45. Schüttelkopf, A. W. & van Aalten, D. M. F. PRODRG: a tool for high-throughput crystallography of protein–ligand complexes. *Acta Crystallogr D Biol Crystallogr* **60,** 1355–1363 (2004).

Chapter 2:

Farnesyltransferase-mediated Delivery of a Covalent Inhibitor Overcomes Alternative Prenylation to Mislocalize K-Ras

Abstract

Mutationally activated Ras is one of the most common oncogenic drivers found across all malignancies and its selective inhibition has long been a goal in both pharma and academia. One of the oldest and most validated methods to inhibit overactive Ras signaling is by interfering with its post-translational processing and subsequent cellular localization. Previous attempts to target Ras processing led to the development of farnesyltransferase inhibitors, which were successful in pre-clinical studies focused on H-Ras but failed in the clinic due to the ability of K-Ras to bypass farnesyltransterase inhibition though alternative prenylation by geranylgeranyltransferase (GGTase). Here we present the discovery of a new generation of electrophillic farnesyltransferase inhibitors that use farnesyltransferase to covalently modify the C-terminal tail of K-Ras *in vitro* and prevent its proper localization in cells.

Introduction

The ability to associate with membranes is a critical feature for the cellular localization and activity of many proteins[1,2]. Early studies of the Ras oncogene highlighted these features when deletions localized to the C-terminal tail were found to prevent its membrane localization, which in turn prevented the ability of oncogenic Ras mutants from transforming cells[3]. Further work isolated the cysteine residue 4 amino acids from the C-terminal end, which is conserved in all Ras proteins, as necessary for their membrane localization[4]. Although this cysteine was initially thought to be palmitoylated, similarities between the Ras family and the known farnesyl modified yeast mating hormone **a**-factor, including similar C-terminal residues and various genetic and pharmacological manipulations indicating they shared the same post-translational

modification (PTM) pathway, helped to experimentally establish that the C-terminal cysteine of Ras was covalently modified with a farnesyl group[5-9].

This finding helped to establish a new class of prenylated proteins named after their 4 C terminal amino acids that conform to a CaaX motif, where the prenylated cysteine is followed by 2 aliphatic residues and a final residue that determines which lipid group is preferentially attached to the cysteine. This motif was found to be sufficient to signal for the covalent attachment of either a farnesyl or geranylgeranyl lipid group by either farnesyltransferase (FTase) or geranylgeranyltransferase (GGTase) respectively to the targeted cysteine[2]. This alkylation is then followed by the cleavage of the 3 terminal amino acids and methylation of the new c-terminal carboxyl group to create a hydrophobic C-terminus suitable for interacting with membranes[10-14].

Intriguingly, it was found that when a small peptide mimicking the final amino acid tail of Ras was injected into cells it could competitively inhibit farnesylation of the full length oncogenic Ras protein, which prevented its membrane localization and ability to activate downstream signaling pathways[15]. This opportunity to therapeutically target the oncogenic Ras protein, found in roughly 16% of all cancers[16], triggered the development of numerous potent peptidomimetic farnesyltransferase inhibitors (FTI) that looked exceptional in the examined pre-clinical models with robust inhibition of Ras's transforming ability and no obvious dose limiting toxicities[17,18].However, in the clinic all of the FTI's tested failed to show a significant benefit over the control arms [19-21].

This un-anticipated failure was largely attributed to several previously unknown differences in the processing of the various Ras isoforms. K-Ras4b (hereafter referred to as K-Ras) was found to bind to FTase more strongly than H-Ras, which was the focus of a majority of

the pre-clinical studies carried out, making it more difficult for the FTI to out compete K-Ras[22]. Additionally, while H-Ras is solely a substrate of FTase, in the presence of an FTI K-Ras can be alternatively prenylated by GGTase, which allows for proper downstream processing, membrane localization, and signaling[22-24]. This new biology helped to explain the clinical failures of FTI's, which were focused in colon and pancreatic cancers that are largely comprised of K-Ras mutant tumors[16]. These difficulties, both biological and in the clinic, led to the disinterest in targeting Ras localization as a therapeutic strategy and left the mythos of the "un-druggable" nature of the Ras oncogene intact.

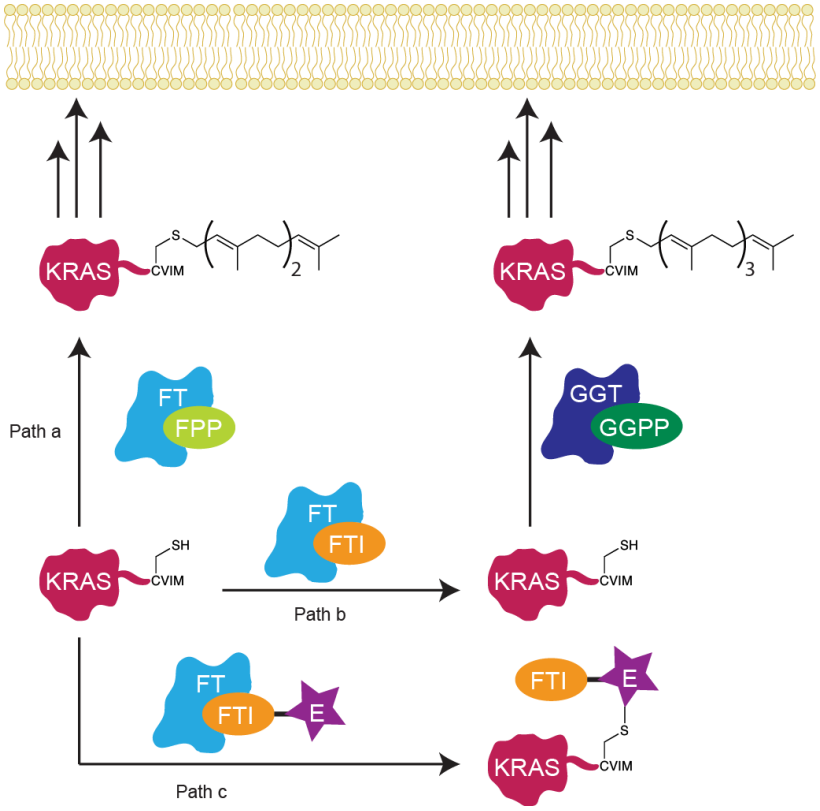

Figure 2.1. Proposed method to overcome innate resistance to K-Ras PTM inhibition. **Path a** depicts the normal course of K-Ras posttranslational modification by FTase, which leads to membrane localization after several subsequent steps. **Path b** shows the scenario when the active site of FTase is blocked with an FTI: a second prenylation enzyme, GGTase, can catalyze geranylgeranylation of K-Ras, which still leads to properly localized and functional K-Ras. **Path c**

represents our proposed approach: proper incorporation of a cysteine-reactive chemical electrophile (e) into an FTI could allow FTase to irreversibly transfer a covalent inhibitor to the normally prenylated cysteine, thereby blocking any other modification at the site and causing mislocalization of K-Ras.

Here we re-visit the idea of functionally inhibiting K-Ras by targeting its PTM's. We envisioned using an electrophilic FTI that could be delivered by FTase to the CaaX motif of Ras where it would be able to covalently modify the target cysteine. This modification could prevent subsequent processing steps while simultaneously blocking alternative prenylation resulting in the mislocalization of Ras to the cytoplasm. The synthesis of such analogs was carried out and the resulting inhibitors were found to covalently modify the CaaX motif of Ras in an FTase dependent manner *in vitro*. Select derivatives were converted to cell permeable pro-drugs that were shown to mislocalize multiple different oncogenic mutants of K-Ras into the cytoplasm and when combined with statins inhibit oncogenic K-Ras signaling. These results suggest that a renewed attempt to inhibit K-Ras PTM's may prove to be a valid strategy towards inhibiting a broad spectrum of Ras oncogenes.

Results

Design and activity of electrophillic farnesyltransferase inhibitors of K-Ras

In designing a next generation FTI for K-Ras inhibition we sought a solution that would circumvent both the issue of K-Ras's high affinity for FTase and it's ability to bypass inhibition through GGTase. We hypothesized that if we could irreversibly label the normally farnesylated cysteine of K-Ras with a small molecule it would prevent all forms of prenylation and prevent the subsequent processing and translocation steps, thereby compromising the ability of K-Ras to signal (Fig. 2.1 path c). Since the C-terminal tail of K-Ras is relatively unstructured with no

obvious nearby pockets for a small molecule inhibitor to derive binding affinity we envisioned harnessing the active site of FTase to deliver the inhibitor to K-Ras.

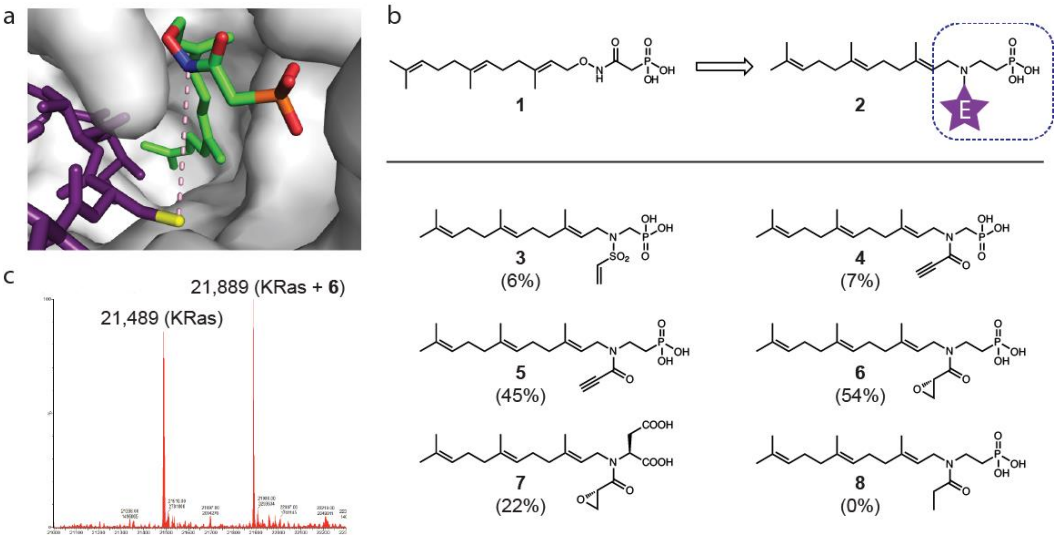

Figure 2.2. Design and *in vitro* activity of eFTI. **a.** The ternary crystal structure of a known reversible inhibitor **1** (green) complexed with FT (gray surface) and the c-terminal tail of K-Ras (purple) (PDB:1D8D) suggests a possible site of attachment for an electrophile on a nitrogen in the inhibitor (blue) towards the target K-Ras cysteine (yellow). **b.** The known reversible inhibitor **1** was adapted into the general scaffold **2** to facilitate incorporation of an electrophile (e) and variation of the electrophile-charged phosphonate "warhead" (dashed box). The structures of eFTI **3**–**7** and non-electrophilic control **8** are shown along with their percent modification of K-Ras in an *in vitro* LC/MS assay (20 µM inhibitor, 10 µM K-Ras, 10 µM FTase, 4 hrs). **c.** Representative LC/MS chromatogram of the reaction between K-Ras and inhibitor **6**. Peaks have been re-labeled for clarity.

As a starting point we analyzed the crystal structure of the farnesyl competitive FTI **1** bound to FTase and the C-terminal peptide of K-Ras (Fig. 2.2a). The chemical structure of **1** was simplified to **2** to allow for the incorporation of an electrophile and facilitate the synthesis of multiple analogs without compromising chemical stability (Fig. 2.2b). A panel of electrophilic farnesyltransferase inhibitors (eFTI) were then synthesized and their ability to covalently label recombinant full-length KRAS in the presence of FTase was determined by intact protein liquid chromatography-mass spectrometry (LC/MS)**.** While some inhibitors showed only modest

labeling (**3** at 6%, Fig 2.2b) the epoxy amide **6** showed substantial labeling of the K-Ras tail. A representative LC/MS chromatogram of K-Ras following the reaction with **6** in the presence of FTase is shown in Fig. 2.2c. Importantly, the analogous experiment without FTase showed completely unmodified K-Ras, indicating that the enzyme was catalyzing the non-natural reaction. Finally, **8**, the desoxy analog of **6**, that lacks the epoxide electrophile was prepared as a negative control and did not show any labeling in the *in vitro* assay.

6* Mislocalizes m-Cerulean K-Ras (G12C)

In order to evaluate the cellular activity of the phosphonate containing compounds we masked the phosphonate moiety of compound 6 and the negative control 8 as a di-pivalate ester pro-drug (referred to as **6*** and **8***). We then evaluated the ability of the cell permeable **6*** and **8*** to mis-localize a dox inducible mCerulean K-Ras containing the oncogenic mutation G12C (mCerulean K-Ras (G12C)). A 9h induction of m-Cerulean K-Ras showed that the labeled K-Ras was properly processed and trafficked to the periplasmic membrane (fig. 2.3a). Treatment of cells with the HMG Co-A reductase inhibitor lovastatin, which prevents the cellular synthesis of both the farnesyl-pyrophosphate and geranylgeranyl pyrophosphate co-factors, thus acting as a dual FTase and GGTase inhibitor, prevented this accumulation at the membrane as did **6***. In contrast, the non-electrophilic inhibitor **8*** had no effect on the localization of K-Ras.

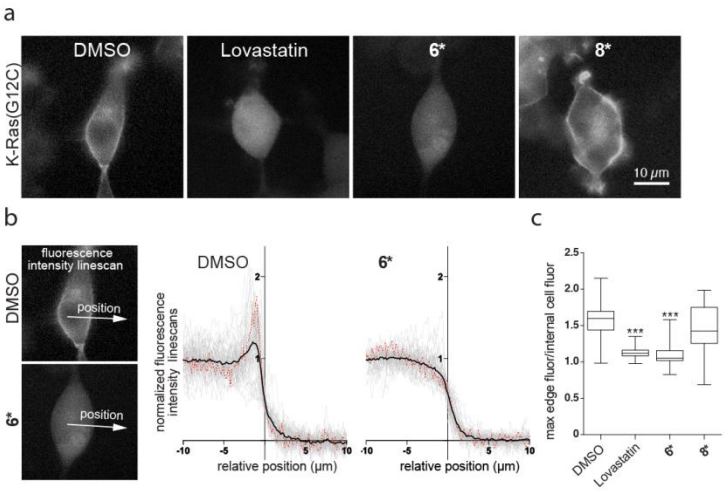

Figure 2.3. 6* displaces K-Ras(G12C) from the plasma membrane. **a**. Representative images showing the localization of mCerulean-K-Ras (G12C) in 293 cells after 9 hours of treatment with DMSO, Lovastatin, **6*** or **8*** (25μM). Bar=10μm. **b**. Fluorescence intensity linescans were measured across the edge of cells as depicted by the arrows overlaid on the fluorescence images. Aligned and normalized intensity linescans (see Materials and Methods) are plotted for cells treated with DMSO or **6*** (n=50, gray lines). The average linescan for each population (black line) and linescans corresponding to the cells shown on the fluorescence images (dashed red line) are highlighted in the graphs. **c**. The ratio of the maximum edge fluorescence to internal cellular fluorescence was calculated for each cell (see Materials and Methods) and summarized in box and whiskers plots for each population of cells (n=50). Whiskers correspond to min/max values. Statistically significant differences between DMSO- and drug-treated cells were calculated using the Mann-Whitney test (****p*<0.0001).

In order to quantify the degree of K-Ras mislocalization we measured the fluorescence intensity of the labeled K-Ras across a linescan spanning from a cells cytoplasm towards the extracellular space. We then applied a sigmoidal fit to the fluorescent signal that was used to align all scans at the sigmoidal midpoint i.e. the membranes edge. A representative example for cells treated either with DMSO or **6*** is shown in figure 2.3b with the linescan shown as an arrow and the resulting trace highlighted in red. Linescans were generated from 50 cells per condition each shown in gray. The ratio of membrane localized K-Ras to cytoplasmic K-Ras was calculated

(representative example in Fig. 2.4) demonstrated that **6*** but not the non-electrophilic **8*** is capable of mis-localizing oncogenic K-Ras into the cytoplasm as effectively as the positive control compound lovastatin (Fig 2.3c)

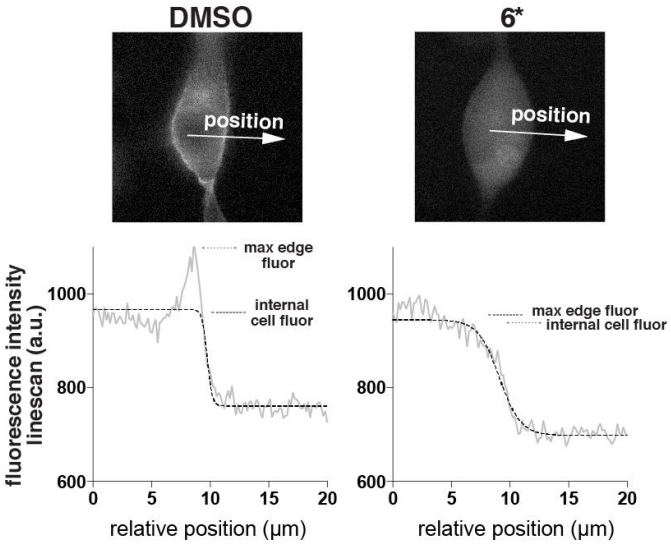

Figure 2.4. Representative example of the values taken to calculate the cytoplasmic and membrane fluorescence for a cell treated with either DMSO or **6***.

6* Prevents K-Ras bypass of FTase and Mislocalizes K-Ras

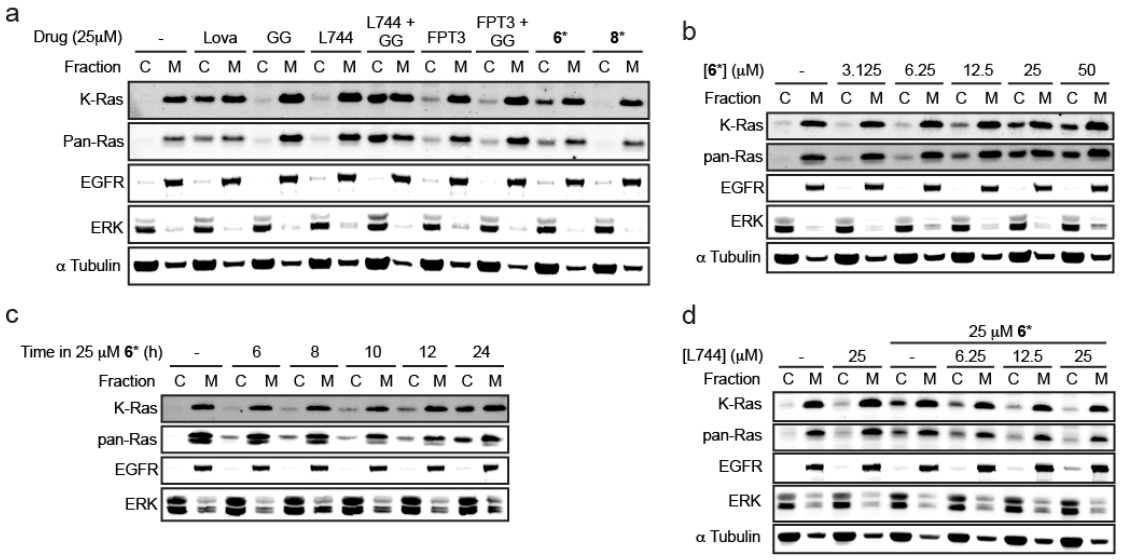

Figure 2.5. 6* mislocalizes oncogenic K-Ras into the cytoplasm. **a**. PSN-1 cells (K-Ras G12R) were treated with the indicated inhibitors for 24 h and the lysates were separated into cytoplasmic (C) and membrane (M) fractions. K-Ras can bypass both the peptide competitive and farnesyl pyrophosphate competitive FTase inhibitors through GGTase in order to maintain its proper localization. In contrast, **6*** induces the mislocalization of K-Ras to the cytoplasm. Lova = Lovastatin, inhibits FTase and GGTase by blocking cellular synthesis of their activated prenylation substrates, GG = GGTI 298, peptide competitive GGTase inhibitor, L744 = L744,832 peptide competitive FTase inhibitor, FPT3 = FPT III, farnesyl pyrophosphate competitive inhibitor, the pro-drug version of **1. b. 6*** inhibits the membrane localization of K-Ras in a dose dependent manner at 24h. **c**. The mislocalization of K-Ras by **6*** is time dependent. **d**. Cellular fractionation of PSN-1 cells treated with either L744, **6***, or **6*** in the presence of increasing concentrations of L744 show the cellular activity of **6*** is dependent on K-Ras binding to FTase.

We next evaluated the ability of our inhibitors in the PSN-1 cell line, which contains a G12R K-Ras mutation and has previously been shown to bypass FTase inhibition[25]. Cellular fractionation validated that K-Ras could escape both a peptide competitive, L744,832 (L744), or a farnesyl pyrophosphate competitive ,FPT inhibitor III (FPT3), FTI and maintain its proper membrane localization. However, targeting both FTase and GGTase using either lovastatin (Lova) or the GGTase inhibitor, GGTI 298 (GG), in addition to the peptide competitive FTase

inhibitor(L744+GG) resulted in robust mislocalization of K-Ras to the cytoplasm (Fig. 2.5a). Similar to the dual inhibitor treatment and consistent with the fluorescently tagged Ras system **6*** but not **8*** was able to successfully alter the localization of K-Ras to the cytoplasm (Fig. 2.5a). This activity was both time and dose dependent (Fig. 2.5b, c) and was also seen in SW-620 cells, which contain the G12V K-Ras mutation (Fig. 2.6). To verify that the eFTI's cellular activity was dependent on FTase as it was *in vitro* and not an artifact of the electrophile we treated cells with either **6*** alone or in combination with increasing doses of the peptide competitive FTase inhibitor. Hypothesizing that the peptide competitive FTase inhibitor would prevent K-Ras from coming into contact with the **6** + FTase complex and allow it to bypass the eFTI through GGTase. As shown in figure 2.5d this co-treatment strategy was effective in preventing the mislocalization of K-Ras into the cytoplasm indicating that the cellular ability of **6*** to mislocalize K-Ras is dependent on FTase.

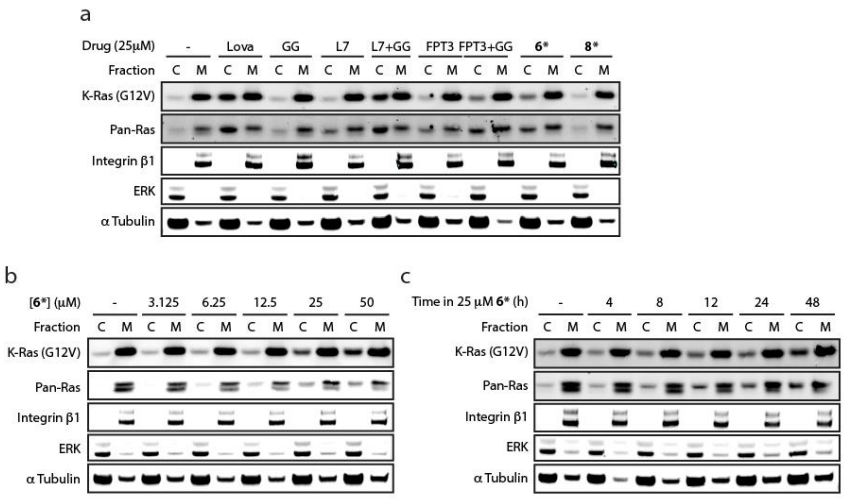

Figure 2.6.. **6*** is active against other oncogenic variants of K-Ras. **a**. The cellular localization of K-Ras was evaluated in SW-620 cells (KRAS G12V) treated with the indicated inhibitors for 24h. **b. 6*** inhibits the membrane localization of K-Ras in a dose dependent manner at 24h. **c**. The mislocalization of K-Ras by **6*** is time dependent.

To evaluate the effect of mislocalizing K-Ras from the membrane on MAPK signaling we probed p-ERK levels in PSN-1 cells after a 24h after treatment with a dose response of **6***. While these concentrations were sufficient to mislocalize a substantial portion of K-Ras to the cytoplasm at this timepoint, p-ERK remained un-inhibited. This lack of activity could potentially be due to the increased expression of K-Ras that keep the level of membrane bound K-Ras consistent despite a substantial quantity now residing in the cytoplasm (Fig 2.5b, c, 2.7a).

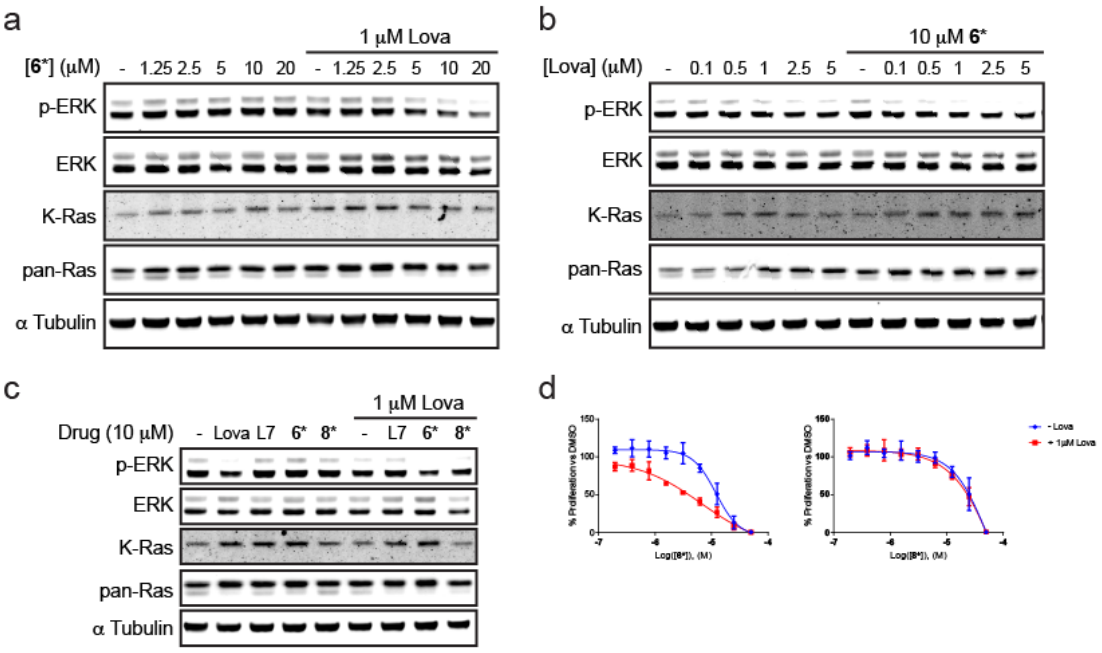

Figure 2.7. **6*** in combination with statins can inhibit K-Ras signaling and proliferation. **a-c**. PSN-1 cells were treated with the indicated inhibitors for 24h and whole cell lysates were analyzed by the given antibodies. **d**. 72h proliferation of PSN-1 cells against a dose response of either 6* or 8* +/- 1 μM Lova (mean ± S.D., n=2).

Previous studies have shown that statins, which decrease the cellular concentration of farnesyl pyrophosphate, can increase the potency of farnesyl pyrophosphate competitive FTI's such as **6*** by allowing them to more effectively compete for the FTase active site. The co-

treatment of cells with 1 μM of Lovastatin plus **6*** was sufficient to inhibit p-ERK signaling (Fig. 2.7a). The reverse combination experiment also showed that the addition of 10 μM **6*** to a dose response of lovastatin also increased its ability to inhibit p-ERK (Fig. 2.7b). This increased activity was specific to the electrophilic compound **6*** and not **8*** or the peptide competitive FTase inhibitor (Fig. 2.7c) and also resulted in an increase in the anti-proliferative ability of **6*** in PSN-1 cells (Fig. 2.7d).

Discussion

The term "undruggable target" serves as a placeholder until strategies are developed to overcome the unique challenges associated with the molecular recognition of proteins by small molecules that alter their biological output. While considerable effort has focused on how to drug structurally defined protein domains that lack obvious small molecule binding pockets a less studied category of "undruggable" domains are those with little or no stable tertiary structure. The most notorious example of an undruggable protein in oncology, oncogenic K-Ras, possesses two structural domains that typify each category. The structured G-domain responsible for engaging with effectors and initiating downstream signaling and the flexible C-terminal tail responsible for membrane localization. Recently, the G-domain has been successfully targeted by exploiting the unique chemical reactivity of the oncogenic G12C mutation[26-28]. Here, we developed a novel chemical strategy to target the flexible C-terminal tail of K-Ras by taking advantage of its known biology to identify an interacting partner that offered a small molecule binding pocket that we could use to deliver our inhibitor in a targeted manner.

Previous generations of inhibitors targeting K-Ras localization focused solely on inhibiting the function of FTase itself leaving the translated K-Ras CaaX motif available for

prenylation by GGTase, which is sufficient for downstream processing and K-Ras localization. By directly targeting the cysteine side chain we were able to overcome this innate resistance mechanism and mislocalize K-Ras to the cytoplasm with a single agent. Other groups have previously tried to mislocalize K-Ras using un-natural farnesyl derivatives, but the resulting inhibitors were either non-cell permeable, or required high concentrations of an alcohol precursor that relied on subsequent cellular processing to form the necessary un-natural farnesyl pyrophosphate[29-31].

The clinical failure of FTI's led to an abandonment of the therapeutic area. However, there is renewed interest in FTI's that may lack efficacy against K-Ras have been verified to be potent inhibitors of H-Ras and are currently being tested in clinical trials of patients harboring tumors with oncogenic H-Ras mutations[32]. These may soon lead to the long awaited breakthrough of Ras inhibitors, which our data suggests could eventually be expanded to a broader patient population harboring K-Ras mutations.

Methods

Cell Culture and Reagents. PSN-1 and SW-620 cells were purchased from ATCC. PSN-1 cells were maintained in RPMI-1640 (Gibco) + 10% FBS at 37°C and 5% CO_2. SW-620 cells were maintained in Leibovitz's L-15 (Gibco) + 10% FBS at 37°C.

Anti-ERK (cat#4695), anti-α-tubulin (cat#3873), anti-EGFR (cat#4267), anti-pan-Ras (cat #3965), anti-K-Ras(G12V) (cat#14412) were purchased from cell signaling technologies, Anti-integrin β1 (ab134179) was purchased from Abcam, anti-K-Ras (sc-30) was purchased from

Santa-Cruz biotechnology. All antibodies were used at a 1:1000 dilution except for anti-pan-Ras (1:500), and anti K-Ras (1:200)

L744,832 was purchased from Enzo Life Sciences, FPT inhibitor III was purchased from Millipore, GGTI 298 was purchased from Tocris. All inhibitors were aliquoted and stored as 25mM DMSO stocks at -20°C.

In vitro LC/MS assay for FTase-mediated KRAS modification. Each inhibitor (20 μM) was incubated with FTase (10 μM) and KRAS4B (20 μM) in a buffer consisting of 50 mM Tris pH 7.4, 5 mM $MgCl_2$, 20 mM KCl, 50 μM $ZnCl_2$, 2 mM DTT, with a final DMSO concentration of 2%. Reactions were run for 4 h, then were analyzed by LC/MS using a C4 column and protein MS method.

Cell line generation. This procedure was carried out by Cairn Biosciences. FLAG-mCerulean-KRas (G12C) and Venus-CRaf constructs were cloned into a tetracycline-inducible bicistronic expression vector. A stable cell line was generated by co-transfecting Flp-In TREx 293 cells (Life Technologies) with the bicistronic vector and Flp-recombinase expression plasmid pOG44 (Life Technologies) at a ratio of 1:3 using FuGENE6 (Promega) followed by selection with 75μg/ml hygromycin B. Flp-In TREx 293 cells were were maintained in DMEM/F-12 1:1, 10% Tet-free FBS, GlutaMAX with 15μg/ml blasticidin and 100μg/ml Zeocin, while the media for stably transfected cells included 15μg/ml blasticidin and 75μg/ml hygromycin B. Cell culture reagents and antibiotics were purchased from Life Technologies.

Microscopy and image analysis. This procedure was carried out by Cairn Biosciences. FLAG-mCerulean-KRas (G12C)/Venus-CRaf TREx-293 stable cells were seeded onto glass-bottom 96-well SensoPlate Plus microplates (Greiner Bio-One) at a density of 3 or $5x10^4$ cells/well and

allowed to incubate overnight without antibiotics. Cells were then simultaneously treated with 1µg/ml doxycyline to induce fluorescent reporter expression and 25µM Lovastatin, 25µM **6***, 25µM **8*** or DMSO in triplicates.

Cells were imaged after 9 hours using an inverted Nikon Ti-E microscope (located at the Nikon Imaging Center, UCSF) equipped with an OKOLab cage incubator system and Hamamatsu ORCA Flash 4.0 camera. Images were acquired using a Plan Fluor 40x/0.75 (DIC N2 / 40X I) objective and NIS-Elements software.

A total of 50 cells for each treatment from at least 3 wells from 2 independent experiments carried out on separate days were analyzed. Fluorescence intensity profiles (linescans) across the edge of cells were measured using FIJI (ImageJ) by manually drawing a line (5-pixel width) normal to the membrane of each cell. These linescans were fitted with sigmoid functions and aligned along the x-axis using the sigmoid's midpoint. The maximum edge fluorescence value was calculated as the highest intensity value within 30(pixel)*0.1625(µm)=4.875µm of the cell boundary determined by the sigmoid fit. The sigmoid's upper plateau was used as the internal cellular fluorescence value. Ratios of maximum edge fluorescence to internal cellular fluorescence were calculated after subtracting the background values corresponding to the sigmoid's lower plateau for each cell. Intensity values were normalized so that the sigmoid fit fell between 1 and 0 in graphs displaying linescans. GraphPad Prism6 was used to generate graphs and perform statistical comparisons.

Immunoblotting. Cells were grown in 6 well plates and treated according to the indicated conditions at which point the media was aspirated, cells were washed with 1mL of cold PBS, which was then aspirated and the plates were frozen at -80°C. For whole cell extracts the frozen

cells were thawed on the plates in a buffer containing 50mM Tris pH 7.5, 150mM NaCl, 1mM EDTA, and 1% Triton X-100 supplemented with 1x phosphatase (PhoSTOP, Roche) and 1x protease (complete-mini tablets, Roche) inhibitors. Lysates were scraped, transferred to Eppendorf tubes, and cleared by centrifugation at 20,000xg for 20 min at 4°C. The clarified lysates were transferred to chilled, clean tubes, and normalized for protein concentration by Bradford (Bio-Rad). The normalized lysates were diluted with Laemmli loading buffer, and 10µg of total protein was run on a 4-12% gradient gel (Invitrogen), which was then transferred to .45 µM nitrocellulose (Bio-Rad) and analyzed using the indicated primary antibodies according to the manufacturer's recommendations. Primary antibodies were detected using IRDye secondary antibodies (Li-Cor) according to the manufacturer's recommendations and scanned on an Odyssey imager (Li-Cor). Scanned images were cropped and assembled in Adobe Illustrator 6. Fractionated lysates were generated using the Mem-PER Plus Membrane Protein Extraction Kit (Thermo-Fisher) using the manufacturers recommended protocol scaled down for a 6 well plate.

Proliferation Assays. PSN-1 cells were plated onto opaque white 96-well plates (Greiner cat#655083) and allowed to adhere overnight. The following day media was changed to fresh media that contained either DMSO or the indicated concentration of drug plus 1 µM Lova as indicated. Plates were incubated at 37°C for 72h and cell viability was read out using CellTiter-Glo assay (Promega) according to the manufacturer's protocol. Proliferation was normalized to the DMSO control condition and plotted in GraphPad Prism 6 and fit with a non-linear regression of the log(inhibitor) vs response with a variable slope where shown. Graphs show the averages (+/- standard deviation) of biological duplicates each performed in technical triplicate.

Chemical Synthesis. All Synthesis was designed and performed by Gregory Hamilton, a postdoc in the Shokat lab at UCSF the details of which can be found in the acknowledged manuscript that is in preparation.

References

1.Konstantinopoulos, P. A., Karamouzis, M. V. & Papavassiliou, A. G. Post-translational modifications and regulation of the RAS superfamily of GTPases as anticancer targets. *Nature Reviews Drug Discovery* **6,** 541–555 (2007).

2.Wang, M. & Casey, P. J. Protein prenylation: unique fats make their mark on biology. *Nature Reviews Molecular Cell Biology* **17,** 110–122 (2016).

3.Willumsen, B. M., Christensen, A., Hubbert, N. L., Papageorge, A. G. & Lowy, D. R. The p21 ras C-terminus is required for transformation and membrane association. *Nature* **310,** 583–586 (1984).

4.Willumsen, B. M., Norris, K., Papageorge, A. G., Hubbert, N. L. & Lowy, D. R. Harvey murine sarcoma virus p21 ras protein: biological and biochemical significance of the cysteine nearest the carboxy terminus. *EMBO J* **3,** 2581–2585 (1984).

5.Anderegg, R. J., Betz, R., Carr, S. A., Crabb, J. W. & Duntze, W. Structure of Saccharomyces cerevisiae mating hormone a-factor. Identification of S-farnesyl cysteine as a structural component. *Journal of Biological Chemistry* **263,** 18236–18240 (1988).

6.Powers, S. *et al.* RAM, a gene of yeast required for a functional modification of RAS proteins and for production of mating pheromone a-factor. *Cell* **47,** 413–422 (1986).

7.Schafer, W. R. *et al.* Genetic and pharmacological suppression of oncogenic mutations in ras genes of yeast and humans. *Science* **245,** 379–385 (1989).

8.Hancock, J. F., Magee, A. I., Childs, J. E. & Marshall, C. J. All ras proteins are polyisoprenylated but only some are palmitoylated. *Cell* **57,** 1167–1177 (1989).

9.Casey, P. J., Solski, P. A., Der, C. J. & Buss, J. E. p21ras is modified by a farnesyl isoprenoid. *Proceedings of the National Academy of Sciences* **86,** 8323–8327 (1989).

10.Clarke, S., Vogel, J. P., Deschenes, R. J. & Stock, J. Posttranslational modification of the Ha-ras oncogene protein: evidence for a third class of protein carboxyl methyltransferases. *Proceedings of the National Academy of Sciences* **85,** 4643–4647 (1988).

11.Hrycyna, C. A., Sapperstein, S. K., Clarke, S. & Michaelis, S. The Saccharomyces cerevisiae STE14 gene encodes a methyltransferase that mediates C-terminal methylation of a-factor and RAS proteins. *EMBO J* **10,** 1699–1709 (1991).

12.Otto, J. C., Kim, E., Young, S. G. & Casey, P. J. Cloning and characterization of a mammalian prenyl protein-specific protease. *Journal of Biological Chemistry* **274,** 8379–8382 (1999).

13.Kim, E. *et al.* Disruption of the mouse Rce1 gene results in defective Ras processing and mislocalization of Ras within cells. *Journal of Biological Chemistry* **274,** 8383–8390 (1999).

14.Boyartchuk, V. L., Ashby, M. N. & Rine, J. Modulation of Ras and a-factor function by carboxyl-terminal proteolysis. *Science* **275,** 1796–1800 (1997).

15.Kim, R., Rine, J. & Kim, S. H. Prenylation of mammalian Ras protein in Xenopus oocytes. *Molecular and Cellular Biology* **10,** 5945–5949 (1990).

16.Prior, I. A., Lewis, P. D. & Mattos, C. A Comprehensive Survey of Ras Mutations in Cancer. *Cancer Research* **72,** 2457 (2012).

17.James, G. L. *et al.* Benzodiazepine peptidomimetics: potent inhibitors of Ras farnesylation in animal cells. *Science* **260,** 1937–1942 (1993).

18.Kohl, N. E. *et al.* Selective inhibition of ras-dependent transformation by a farnesyltransferase inhibitor. *Science* **260,** 1934–1937 (1993).

19.Berndt, N., Hamilton, A. D. & Sebti, S. M. Targeting protein prenylation for cancer therapy. *Nature Reviews Cancer* **11,** 775–791 (2011).

20.Van Cutsem, E. *et al.* Phase III trial of gemcitabine plus tipifarnib compared with gemcitabine plus placebo in advanced pancreatic cancer. *Journal of Clinical Oncology* **22,** 1430–1438 (2004).

21.Rao, S. *et al.* Phase III double-blind placebo-controlled study of farnesyl transferase inhibitor R115777 in patients with refractory advanced colorectal cancer. *Journal of Clinical Oncology* **22,** 3950–3957 (2004).

22.Fiordalisi, J. J. *et al.* High Affinity for Farnesyltransferase and Alternative Prenylation Contribute Individually to K-Ras4B Resistance to Farnesyltransferase Inhibitors*. *Journal of Biological Chemistry* **278,** 41718 (2003).

23.Whyte, D. B. *et al.* K- and N-Ras are geranylgeranylated in cells treated with farnesyl protein transferase inhibitors. *Journal of Biological Chemistry* **272,** 14459–14464 (1997).

24.Rowell, C. A., Kowalczyk, J. J., Lewis, M. D. & Garcia, A. M. Direct demonstration of geranylgeranylation and farnesylation of Ki-Ras in vivo. *Journal of Biological Chemistry* **272,** 14093–14097 (1997).

25.Lobell, R. B. *et al.* Evaluation of farnesyl:protein transferase and geranylgeranyl:protein transferase inhibitor combinations in preclinical models. *Cancer Research* **61,** 8758–8768 (2001).

26.Ostrem, J. M., Peters, U., Sos, M. L., Wells, J. A. & Shokat, K. M. K-Ras(G12C) inhibitors allosterically control GTP affinity and effector interactions. *Nature* **503,** 548–551 (2013).

27.Lim, S. M. *et al.* Therapeutic targeting of oncogenic K-Ras by a covalent catalytic site inhibitor. *Angew Chem Int Ed Engl* **53,** 199–204 (2013).

28.Patricelli, M. P. *et al.* Selective Inhibition of Oncogenic KRAS Output with Small Molecules Targeting the Inactive State. *Cancer Discovery* **6,** 316–329 (2016).

29.Adams, V. R. *et al.* Anticancer activity of novel unnatural synthetic isoprenoids. *Anticancer Res* **30,** 2505–2512 (2010).

30.Roberts, M. J. *et al.* Hydrophilic anilinogeranyl diphosphate prenyl analogues are Ras function inhibitors. *Biochemistry* **45,** 15862–15872 (2006).

31.Srinivasan, K., Subramanian, T., Spielmann, H. P. & Janetopoulos, C. Identification of a farnesol analog as a Ras function inhibitor using both an in vivo Ras activation sensor and a phenotypic screening approach. *Mol Cell Biochem* **387,** 177–186 (2013).

32.Chen, X., Makarewicz, J. M., Knauf, J. A., Johnson, L. K. & Fagin, J. A. Transformation by Hras(G12V) is consistently associated with mutant allele copy gains and is reversed by farnesyl transferase inhibition. *Oncogene* **33,** 5442–5449 (2013).

Chapter 3:

Design of a Novel HER3 Binder

Having failed to find a small molecule capable of targeting HER3 from our high throughput screen in chapter 1 we sought to introduce biological specificity and functionality into bosutinib, a Src/Abl inhibitor that had been identified in a broad screening panel as having exceptional potency in binding to the HER3 kinase domain[1]. This binding activity was confirmed by crystallography and showed that bosutinib stabilized the HER3 kinase domain in a conformation identical to ATP bound HER3; however no reliable data showed that bosutinib had any biological impact on the function of HER3[2]. We attributed this lack of biological activity to the fact that bosutinib did not disrupt the kinase conformation of HER3 from the one stabilized by its endogenous ligand ATP, which is likely bound to preserve the kinase fold through the hydrophobic catalytic spine[3].

Since both bosutinib and our inhibitor **2** from chapter 1, which most likely stabilizes the "active conformation" of HER3, failed to alter the signaling capabilities of HER3 we hypothesized that either a DFG in/α-C out or Type II HER3 inhibitor may be able to induce a large enough structural re-arrangement to inhibit HER3's ability to activate HER2. Type II inhibitors have previously been used to change the conformation of a kinase in order to alter its dimerization and signaling output[4,5]. Of particular note, cryo EM structures showed that lapatinib was able to stabilize the inactive conformation of EGFR to the extent that inactive homodimers persisted even in the presence of EGF as analyzed by cryo EM[6]. To determine whether a similar effect may be achievable in HER3 we utilized a hybrid inhibitor approach previously used by our lab where a type II binding element is fused to a type I hinge binding element[7]. This approach allows us to take advantage of the extremely tight binding between HER3 and bosutinib that may allow un-optimized type II elements to bind to provide a starting point for additional medicinal chemistry.

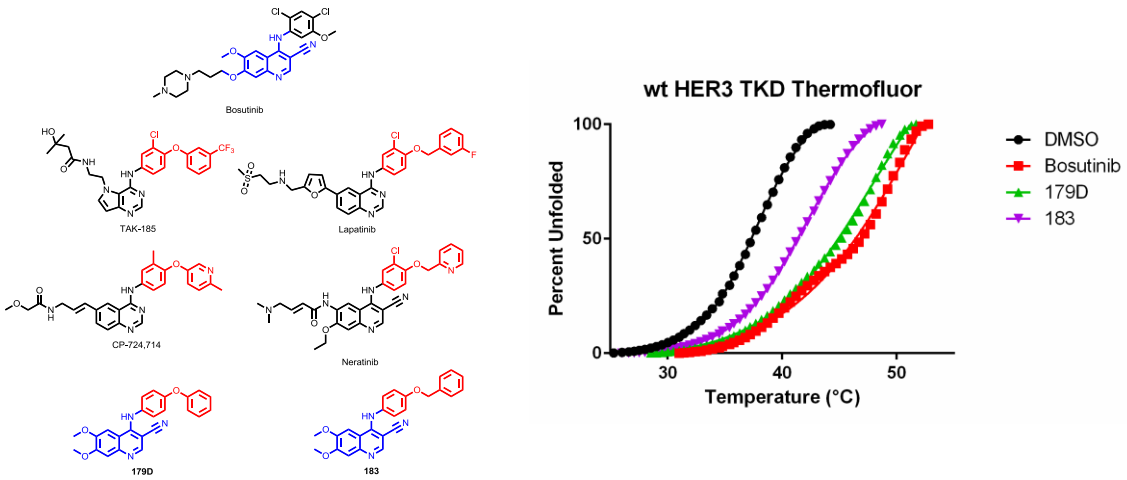

Figure 3.1. a. Chemical structure of bosutinib with its hinge binding element in blue, EGFR family inhibitors that bind to the back hydrophobic pocket with that element in red, and the proposed hybrid inhibitors to bind to the back hydrophobic pocket of HER3, b. Melting temperature of the HER3 kinase domain as measured by thermofluor in the presence of the indicated compounds.

Analysis of existing EGFR family inhibitors revealed that while none bind in a type II manner some do take advantage of the conserved hydrophobic back pocket (Fig. 3.1a). These inhibitors showed an extreme preference for either a substituted phenyl or benzyl ether substituent off of an amine linker to the hinge binding element. Simplified versions of these binding elements (red in Fig. 3.1a) were attached to the bosutinib hinge binding element (blue Fig. 3.1a) to create molecules **179D** and **183**. An *in vitro* thermofluor assay showed that both compounds retained the ability to bind tightly to the HER3 kinase domain as significant shifts in the melting temperature comparable to bosutinib were observed (Fig. 3.1b). We next determined the crystal structure of compound **179D** bound to the kinase domain of EGFR. The crystal structure revealed that the compound binds as expected with the phenyl ether projecting back towards the hydrophobic pocket of the kinase. Furthermore, the structure suggested that an amide or urea linked hydrophobic group attached to compound **179D** on the

terminal phenyl ring at either the meta or para position would be able to make all the critical interactions necessary for a type II inhibitor (Fig. 3.2).

Figure 3.2. Crystal structure of **179D** bound to the kinase domain of EGFR.

We synthesized a panel of such inhibitors and found that only substitutions at the meta position were permitted for binding to HER3 with compound **50A** binding most strongly as analyzed by thermofluor (Fig. 3.3). We next sought to verify whether **50A** would have any activity against HER3 signaling in CHL-1 cells, which are dependent on a NRG autocrine loop to activate HER2/HER3 heterodimers. As Fig 3.4 shows, while **50A** did inhibit p-ERK this activity is most likely attributable to the cyano-quinoline scaffolds propensity to inhibit MEK as both of the less derivatized scaffolds show p-ERK inhibition and **50A** shows no inhibition of signaling at the RTK level (Fig. 3.4).

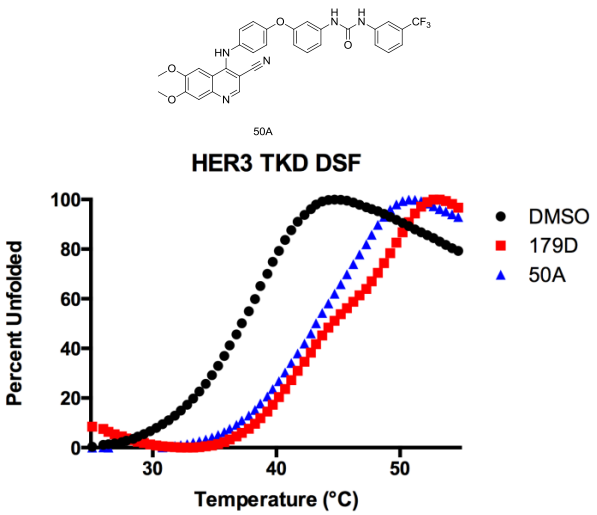

Figure 3.3. **a**.Chemical structure of 50A. **b**. Melting temperature of the HER3 kinase domain as measured by thermofluor in the presence of the indicated compounds.

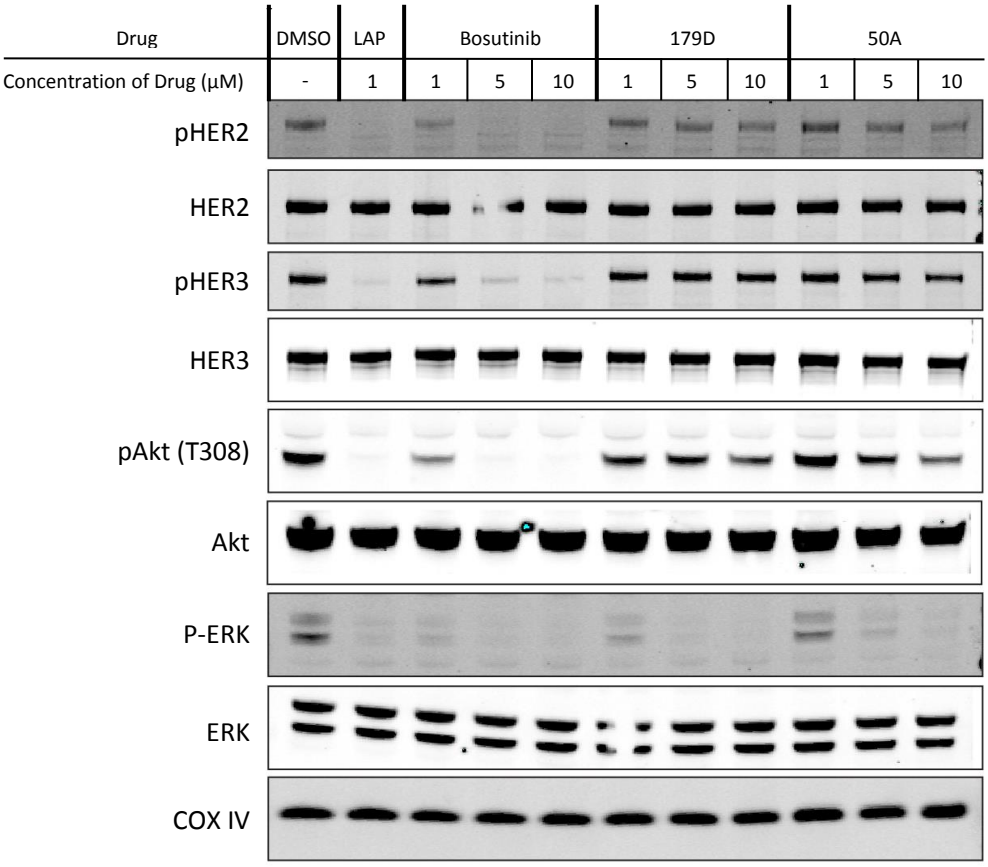

Figure 3.4. Signaling in CHL-1 cells treated with the indicated compounds for 1 hour, LAP is the HER2 inhibitor lapatinib as a positive control for inhibition of p-HER3.

Despite our best efforts we were unable to crystalize **50A** bound to either EGFR or HER3. Since the only crystal structure of our previous inhibitor had been obtained in EGFR, which is known to favor quinazoline scaffolds we hypothesized that attaching the extended type II elements to a quinazoline scaffold would increase the affinity for EGFR such that we could solve the structure to determine if the extended type II elements were indeed stabilizing the DFG out conformation. Thus, compound **73** and several other inhibitors containing the extended type II element on the quinazoline scaffold were synthesized (Fig. 3.5). Intriguingly, all of the

quinazolines with the extended type II element bound to the HER3 kinase domain an activity that is not seen with other quinazoline based EGFR family inhibitors such as lapatinib and gefitinib, and allowed for the crystallization of **73** bound to the active site of EGFR (Fig. 3.5, 3.6)[8]. This crystal structure revealed that while **73** did bind to the back pocket of EGFR the urea linker to the hydrophobic element ran on top of the DFG element as opposed to inducing a flipped conformation. This result made it seem unlikely that we could rationally design a compound that would bind to the EGFR family in a type II manner.

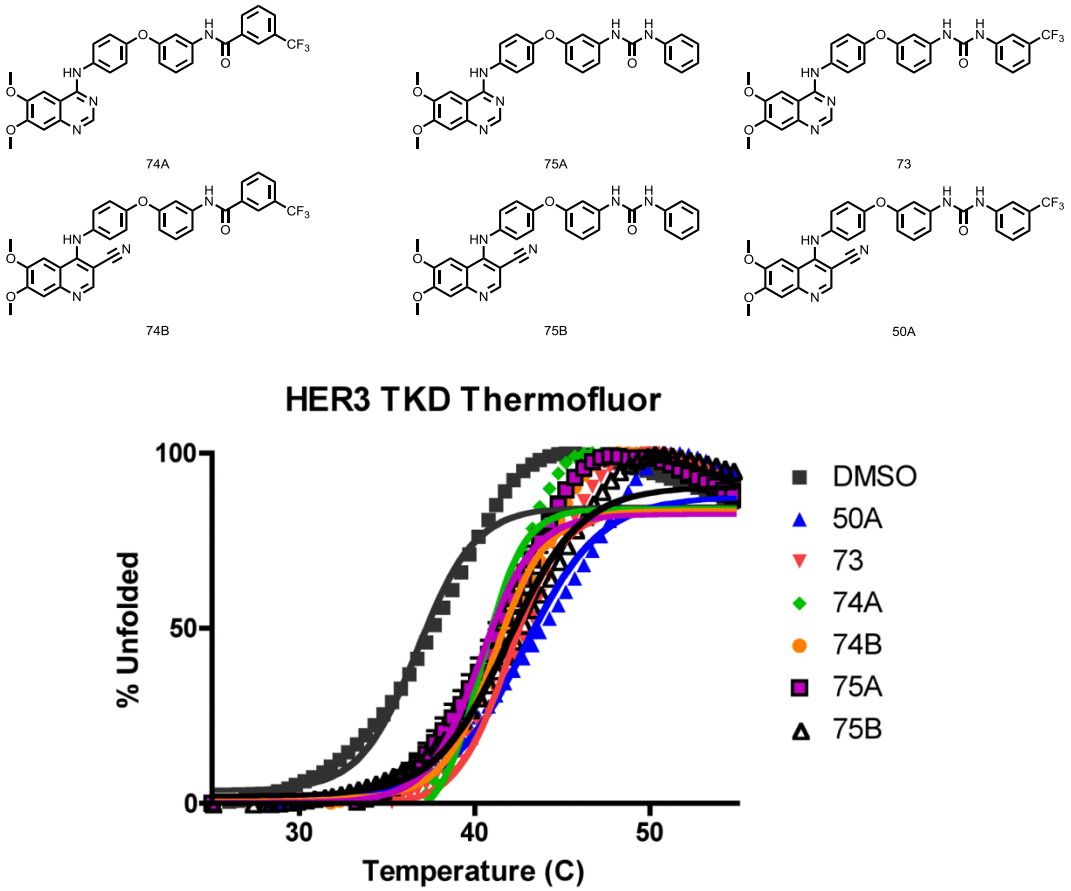

Figure 3.5. Structure and HER3 kinase domain melting curve for extended type II element containing inhibitors

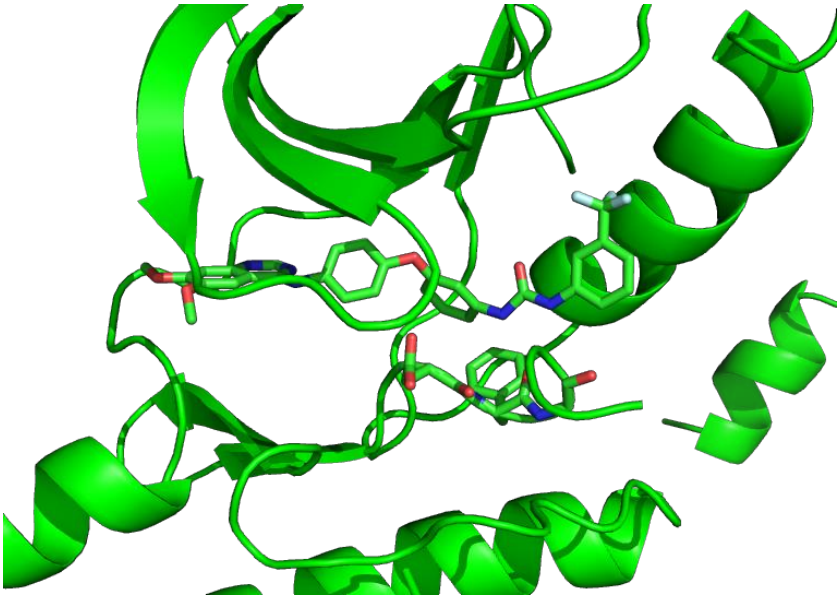

Figure 3.6. Crystal structure of compound **73** bound to EGFR.

We next sought to try to introduce biological activity against HER3 into the bosutinib scaffold by attaching chemical moieties that have previously been reported to recruit E3 ubiquitin ligase complexes to their targets to cause their ubiquitination and degradation. The adamantane containing compound **87** failed to cause the degredation of HER3 in CHL-1 cells and did not inhibit p-ERK as bosutinib does suggesting that it is not cell permeable (Fig. 3.7). Synthesis of the thalidomide containing derivative **8003** also showed no evidence of inducing HER3 degradation (Fig. 3.8). We have since collaborated with a number of established labs to introduce a larger panel of linkers with a degrader element to our HER3 binding element, which will hopefully lead to the first HER3 targeted small molecule.

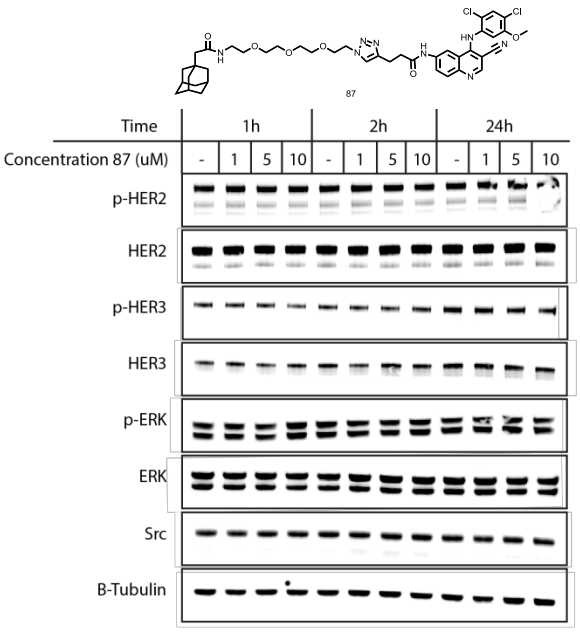

Figrue **3.7**. Chemical structure **87** and western blot of CHL-1 cells treated with **87**.

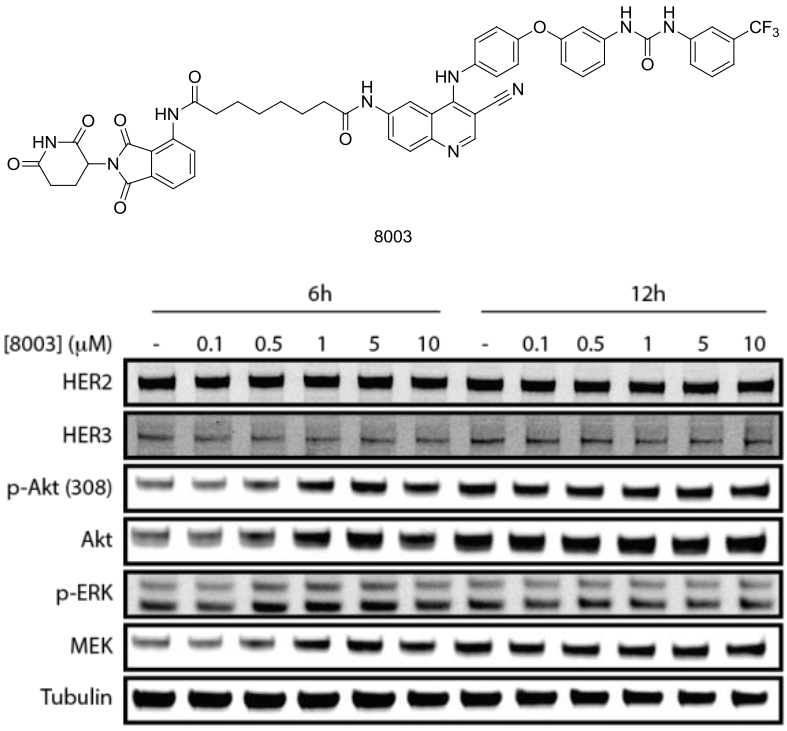

Figure 3.8. Chemical structure of **8003** and western blot of HEK cells treated with **8003**.

Methods

HER3 Thermofluor Assay. Wt HER3 TKD was purified according to the previously published protocol[9]. Thermofluor reactions were performed in duplicate and set up as follows. 1 µL of an inhibitor or DMSO dilution in 40% DMSO:water was added to 19 µL of the HER3 kinase domain in reaction buffer. The final reaction solution contained 100 mM MOPS, 200 mM NaCl, 5% glycerol, 5 mM MgCl2, 0.1 mM DTT, 5x SYPRO Orange, 2 µM kinase, 2% DMSO and 20 µM inhibitor in the wells of a 96-well, low profile, white, PCR plate (USA scientific). The solution was pipetted up and down to mix, sealed with TempAssure clear PCR flat caps (USA Scientific), centrifuged at 500xg for 30 s, and heated in a Stratagene Mx3005P RT-PCR machine from 25°C to 95°C in 0.5°C increments every 30 s after an initial incubation at 25°C for 10 min. Fluorescence was measured at the end of each 30s period with an excitation wavelength of 492 nm and an emission wavelength of 610 nm. To obtain the melting temperature, fluorescent signals were normalized to the maximum fluorescent signal for that well. Values after the well had reached a maximum signal were discarded and the signals were fit to the Boltzmann equation in Graphpad Prism 6. ΔT_m was calculated as the difference in melting temperature between the compound-treated kinase compared to the DMSO control.

Immunoblotting. HEK or CHL-1 cells were grown in 6-well plates and treated according to the indicated conditions at which point the media was aspirated, cells were washed with 1 mL of cold PBS, which was then aspirated and the plates were frozen at -80°C. The frozen cells were thawed on the plates in a buffer containing 50mM Tris pH 7.5, 150mM NaCl, 1mM EDTA, and 1% Triton X-100 supplemented with 1x phosphatase (PhoSTOP, Roche) and 1x protease (complete-mini tablets, Roche) inhibitors. Lysates were scraped, transferred to Eppendorf tubes, and

cleared by centrifugation at 20,000xg for 20 min at 4°C. The clarified lysates were transferred to chilled, clean tubes, and normalized for protein concentration by Bradford (Bio-Rad). The normalized lysates were diluted with Laemmli loading buffer, and 10µg of total protein was run on a 4-12% gradient gel (Invitrogen), which was then transferred to .45 µM nitrocellulose (Bio-Rad) and analyzed using the indicated primary antibodies according to the manufacturer's recommendations (1:1000 antibody dilution). Primary antibodies were detected using IRDye secondary antibodies (Li-Cor) according to the manufacturer's recommendations and scanned on an Odyssey imager (Li-Cor). Scanned images were cropped and assembled in Adobe Illustrator 6.

EGFR Crystalization. EGFR crystal structures were solved in the Jura lab at UCSF.

Chemical Synthesis

General Methods: Reactions were performed in sealed vials with magnetic stirring. All commercial reagents were used without further purification. Silica gel chromatography was performed on a Combiflash Rf + using column cartridges pre-packed with 40-60 micron silica (Teledyne Isco). All RP-HPLC purifications were performed with a Waters 2545 binary gradient module equipped with an XBridge prep C18 column using H2O + 0.1% formic acid and CH3CN + 0.1% formic acid (5-95% gradient) while monitoring at 254 nm. Low resolution mass spectra (LC/ESI-MS) were recorded in positive and negative mode on a Waters TQ detector with an Acquity UPLC equipped with a BEH C18 column.

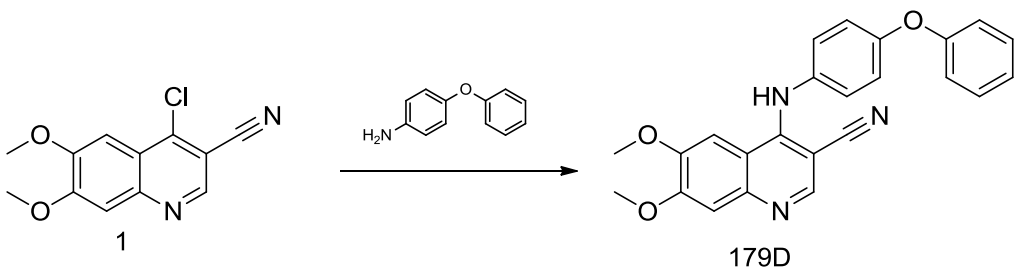

6,7-dimethoxy-4-((4-phenoxyphenyl)amino)quinoline-3-carbonitrile (**179D**). **1** was synthesized as previously reported[10]. 10 mg of **1** and 7.46 mg of 4-phenoxyaniline was added to a vial with a magnetic stir bar. The vial was capped, purged with argon, and 1 mL of 2-ethoxyethanol was added. The vial was heated at 150°C for 3h. The reaction was then cooled and purified by RP-HPLC. Product containing fractions were pooled and dried under reduced pressure to yield 6.4 mg (40%) of **179D** as a yellow solid. MS (ES+) *m/z* 398.3 $(M + H)^+$

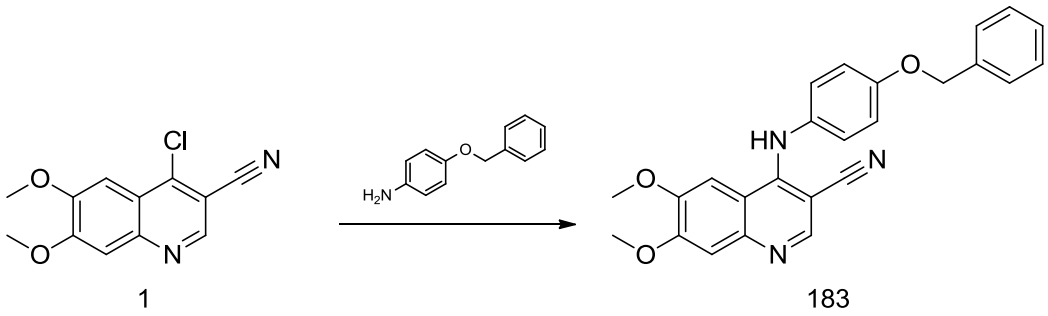

4-((4-(benzyloxy)phenyl)amino)-6,7-dimethoxyquinoline-3-carbonitrile (**183**). **183** was obtained in 61% yield as a yellow solid by a method similar to the one described for compound **179D**. MS (ES+) *m/z* 412.4 $(M + H)^+$

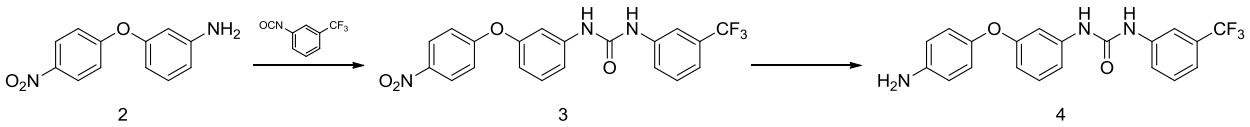

1-(3-(4-aminophenoxy)phenyl)-3-(3-(trifluoromethyl)phenyl)urea (4). **2** was synthesized as previously described[11]. 50 mg of **2** was added to a vial with a stir bar. The vial was capped, purged with argon, and 1 mL of dry dichloromethane was added. The solution was allowed to stir at 0°C for 15 minutes after which 31 µL of 3-(Trifluoromethyl)phenyl isocyanate was added. The reaction was stirred at 0°C for 5 min and was then allowed to warm to 25°C over the course of an hour. The solution was then cooled to -20°C and filtered to yield 69.3 mg of **3** as a crude solid, which was used in the next step without further purification. 44.8 mg of the crude **3** was added to a vial containing 1 mL of THF and a stirbar. 6.0 mg of 10% palladium on carbon was added, the vial was capped and stirred at 25°C under a hydrogen atmosphere for 14h. The reaction was filtered, concentrated *in vacuo* and purified by silica gel chromatography (eluent, 20%EtOAc/Hex to 100% EtOAc) to give 34.4 mg (63% over 2 steps) of **4** as a white solid. MS (ES+) *m/z* 388.3 $(M + H)^{+1}$

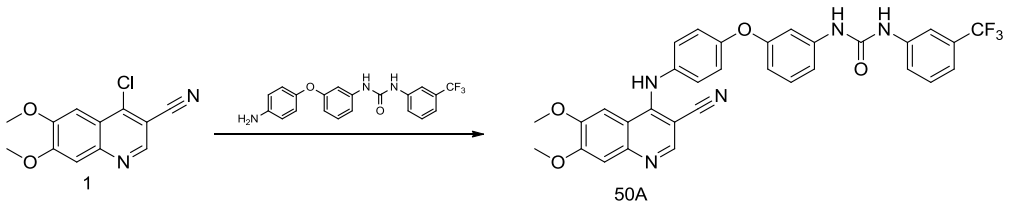

1-(3-(4-((3-cyano-6,7-dimethoxyquinolin-4-yl)amino)phenoxy)phenyl)-3-(3-(trifluoromethyl)phenyl)urea (**50A**). **50A** was obtained in 26% yield as a yellow solid by a method similar to the one described for compound **179D**. MS (ES+) *m/z* 600.3 $(M + H)^{+}$

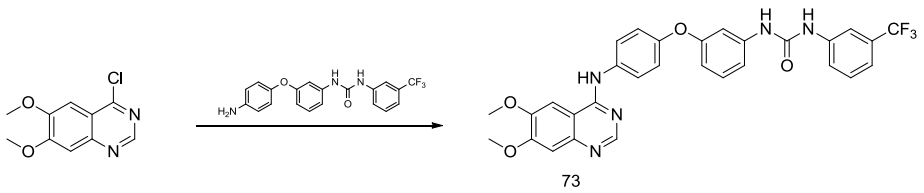

73

1-(3-(4-((6,7-dimethoxyquinazolin-4-yl)amino)phenoxy)phenyl)-3-(3-(trifluoromethyl)phenyl)urea (**73**). 5.8 mg (.025 mmol) of 4-chloro-6,7-dimethoxyquinazoline and 8.5 mg of **4** was added to a vial with a magnetic stir bar. The vial was capped, purged with argon, and 1 mL of isopropanol was added. The vial was heated at 85°C for 1h. The reaction was then cooled to -20°C and the pure product was filtered off to obtain 9.3 mg (63%) of **73** as a yellow solid. MS (ES+) *m/z* 576.2 $(M + H)^+$

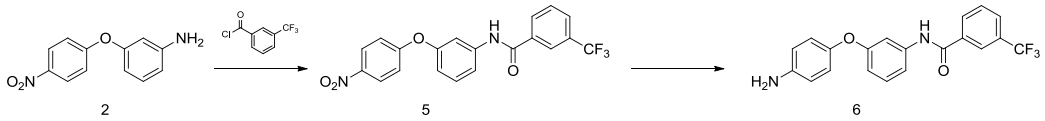

2 5 6

N-(3-(4-nitrophenoxy)phenyl)-3-(trifluoromethyl)benzamide (**6**). 50 mg (.217 mmol) of **2** was added to a vial with a stir bar. The vial was capped, purged with argon, and 1 mL of dry dichloromethane and 0.5 mL of dry DMF was added. The solution was allowed to stir at 0°C for 15 minutes after which 34 µL of 3-(trifluoromethyl)benzoyl chloride was added. The reaction was stirred at 0°C for 5 min and was then allowed to warm to 25°C over the course of an hour. EtOAc and water were then added to the reaction and the organic layer was separated. The aqueous layer was further extracted with 2 aliquots of EtOAc. The organic layers was pooled, washed once with water, once with brine, and reduced *in vacuo*. The crude material was purified by column chromatography (eluent HEX to 30% EtOAc/HEX). Product containing fractions were pooled and reduced *in vacuo* in a vial. 10 mg of 10% palladium on carbon and 1.5

mL of THF was then added to the vial, which was capped and stirred at 25°C under a hydrogen atmosphere for 12h. The reaction was filtered, concentrated *in vacuo* and purified by silica gel chromatography (eluent, 20%EtOAc/Hex to 100% EtOAc) to give 27 mg (31% over 2 steps) of **6**. MS (ES+) *m/z* 373.2 $(M + H)^{+1}$

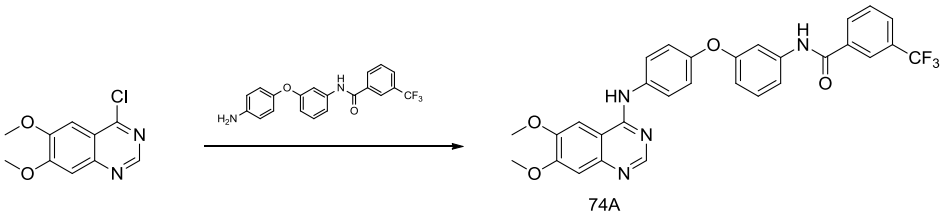

1-(3-(4-((6,7-dimethoxyquinazolin-4-yl)amino)phenoxy)phenyl)-3-(3-(trifluoromethyl)phenyl)urea (**74A**). **74A** was obtained in 85% yield as a yellow solid by a method similar to the one described for compound **73**. MS (ES+) *m/z* 561.2 $(M + H)^{+}$

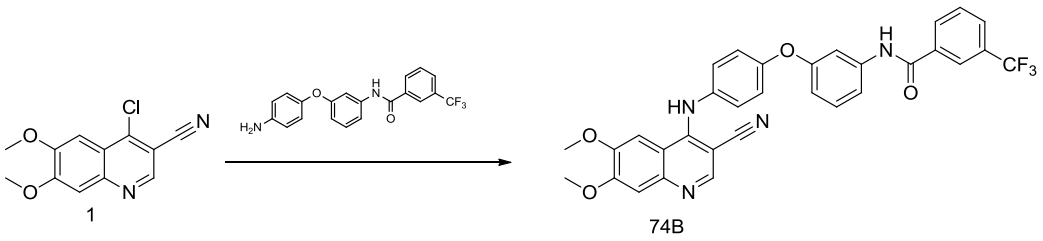

N-(3-(4-((3-cyano-6,7-dimethoxyquinolin-4-yl)amino)phenoxy)phenyl)-3-(trifluoromethyl)benzamide (**74B**). **74B** was obtained in 75% yield by a method similar to the one described for compound **73** using **1** instead of 4-chloro-6,7-dimethoxyquinazoline. MS (ES+) *m/z* 585.2 $(M + H)^{+}$

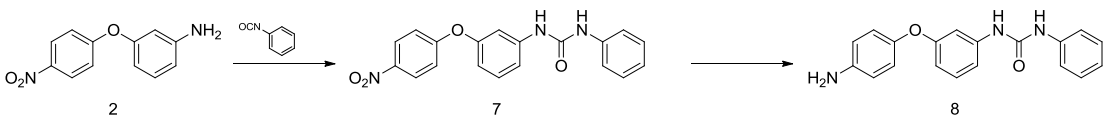

1-(3-(4-aminophenoxy)phenyl)-3-phenylurea (**8**). **8** was obtained in 59% yield over 2 steps by a method similar to the one described for compound **4**. MS (ES+) *m/z* 320.3 $(M + H)^+$

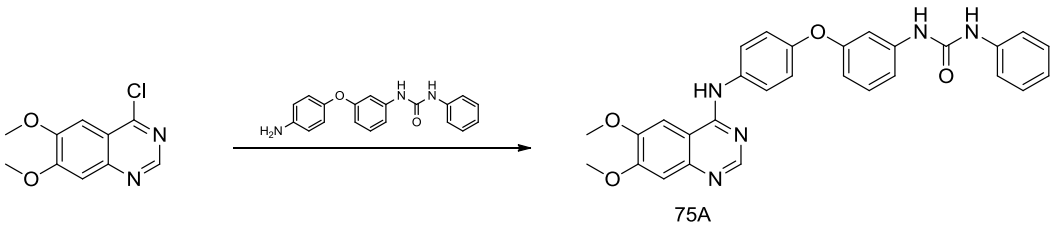

75A

1-(3-(4-((6,7-dimethoxyquinazolin-4-yl)amino)phenoxy)phenyl)-3-phenylurea (**75A**). **75A** was obtained in 83% yield by a method similar to the one described for **73**. MS (ES+) *m/z* 508.2 $(M + H)^+$

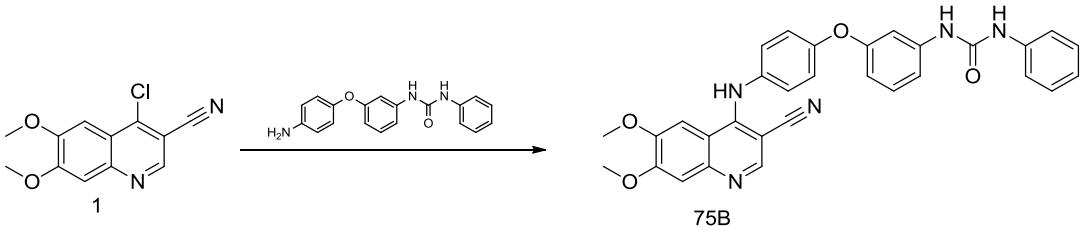

1 75B

1-(3-(4-((3-cyano-6,7-dimethoxyquinolin-4-yl)amino)phenoxy)phenyl)-3-phenylurea (**75B**). **75B** was obtained in 74% yield by a method similar to the one described for **73** using **1** instead of 4-chloro-6,7-dimethoxyquinazoline. MS (ES+) *m/z* 532.2 $(M + H)^+$

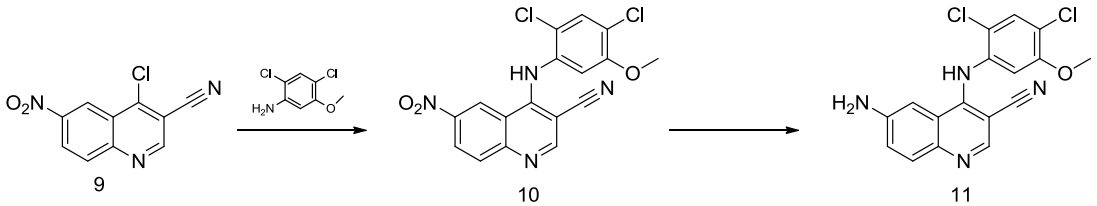

9 10 11

6-amino-4-((2,4-dichloro-5-methoxyphenyl)amino)quinoline-3-carbonitrile (**11**). **9** was synthesized as previously described[12]. 56.5 mg of 2,4-dichloro-5-methoxyaniline was added to a vial containing 62 mg of **9** and 2.5 mL of 2-ethoxyethanol. The vial was capped and heated to 145°C for 2h. The reaction was cooled to rt and reduced *in vacuo.* 2.9 mL of MeOH, 104 mg of iron powder, and 798 µL of 3M ammonium chloride were added to the crude mixture containing **10**, which was refluxed for 1h at 100°C. The reaction was cooled to room temperature, filtered, and reduced *in vacuo*. The crude material was purified by column chromatography (eluent 50%EtOAc/HEX to 100% EtOAc). Product containing fractions were pooled and evaporated under reduced pressure yielding 28 mg (29%) of **11** as a yellow solid. MS (ES+) *m/z* 360.64 $(M + H)^+$

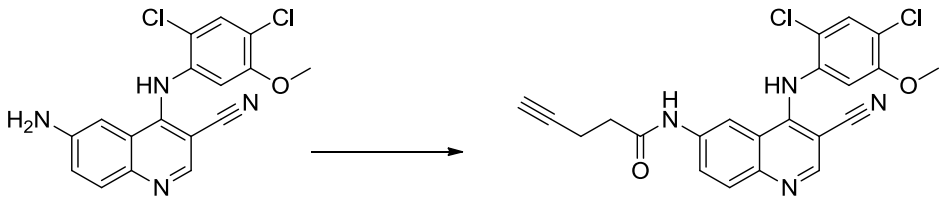

N-(3-cyano-4-((2,4-dichloro-5-methoxyphenyl)amino)quinolin-6-yl)pent-4-ynamide (**12**). 5.2 mg of 4-Pentynoic acid was stirred in 2 mL of a 1:1 mixture of THF and DMF with 6.93 µL of isobutyl chloroformate at 0°C under argon. 5.9 µL of N-methyl morpholine was added and the solution was stirred for 15 minutes. 16 mg of **11** was then added and the reaction was allowed to warm to room temperature overnight. The crude reaction was reduced *in vacuo* and purified by RP-HPLC to yield 8.2 mg (42%) of **12** as a yellow solid. MS (ES+) *m/z* 440.4 $(M + H)^+$

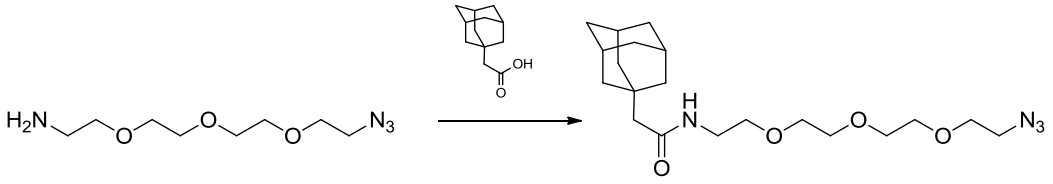

13

2-((3r,5r,7r)-adamantan-1-yl)-N-(2-(2-(2-(2-azidoethoxy)ethoxy)ethoxy)ethyl)acetamide (**13**). 88mg of 1-Adamantaneacetic acid, and 90 µL of 11-Azido-3,6,9-trioxaundecan-1-amine was added to a vial with a stir bar. The vial was capped, purged with argon, and 2.5 mL of dry dichloromethane was added. 83 mg of HOBt and 237 µL of DIPEA was added and the solution was stirred at 0°C for 10 minutes. 104 mg of EDC was added and the reaction was allowed to warm to room temperature overnight. After 12 hours, EtOAc and water were then added to the reaction and the organic layer was separated. The aqueous layer was further extracted with 2 aliquots of EtOAc. The organic layer was pooled, washed once brine, dried with anhydrous MgSO4, which was filtered and reduced *in vacuo*. The crude material was purified by column chromatography (eluent DCM to 10% MeOH/DCM). Product containing fractions were identified by CAM staining on TLC, pooled, and reduced *in vacuo* to give 108 mg (60%) of **13** as a clear oil.

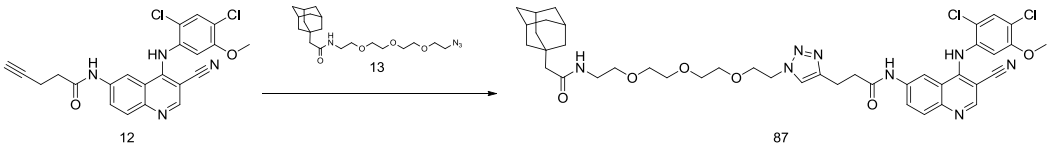

3-(1-(1-((3r,5r,7r)-adamantan-1-yl)-2-oxo-6,9,12-trioxa-3-azatetradecan-14-yl)-1H-1,2,3-triazol-4-yl)-N-(3-cyano-4-((2,4-dichloro-5-methoxyphenyl)amino)quinolin-6-yl)propanamide (**87**). 10 mg of **12** and 9 mg of **13** were added to a vial containing 1 mL of DMF. 22.7 µL of 1M copper sulfate and 27.3 µL of 1 M Ascorbate were added and the reaction was stirred at room

temperature for 1h after which an additional 5.7 µL of 1M copper sulfate and 6.8 µL of 1M ascorbate was added. After 3 hours EtOAc and water were added to the reaction and the organic layer was separated. The aqueous layer was further extracted with 2 aliquots of EtOAc. The organic layers were pooled, washed once brine, dried with anhydrous MgSO4, filtered, and reduced *in vacuo*. The crude material was purified by RP-HPLC. Product containing fractions were pooled and reduced *in vacuo* to give 8.4 mg (44%) of **87** as a yellow oil. MS (ES+) *m/z* 835.0 $(M + H)^+$

74A

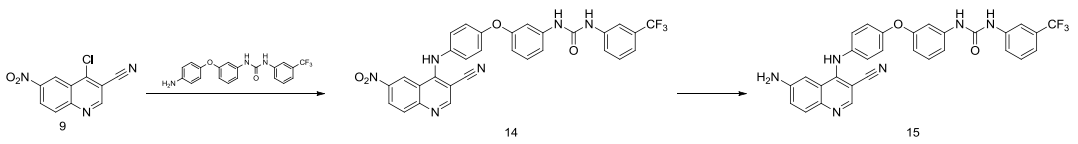

9 14 15

1-(3-(4-((6-amino-3-cyanoquinolin-4-yl)amino)phenoxy)phenyl)-3-(3-(trifluoromethyl)phenyl)urea **(15). 15** was obtained in 37% yield from **9** over 2 steps by a method similar to the one described for **11.** MS (ES+) *m/z* 555.6 $(M + H)^+$

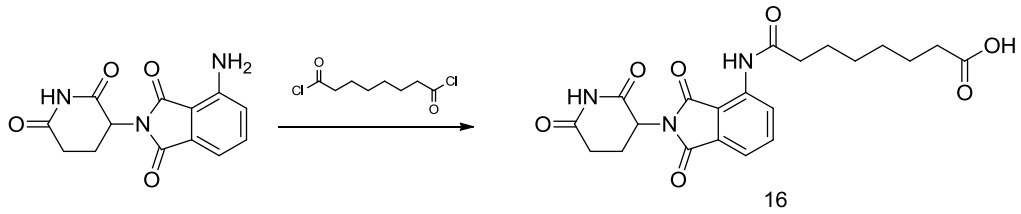

16

8-((2-(2,6-dioxopiperidin-3-yl)-1,3-dioxoisoindolin-4-yl)amino)-8-oxooctanoic acid (**16**). To a flame dried vial with a stir bar 25 mg of pomalidomide was added. The vial was capped and purged with argon and 1.5 mL of dry THF was added. While stirring at 25°C 82 µL of Suberoyl chloride was added dropwise. The reaction was heated to 80°C for 1 hour after which the reaction was cooled to room temperature. Water was added and the reaction was allowed to

stir for 15 minutes. The mixture was then extracted with EtOAc three times. The pooled organic layer was dried with $MgSO_4$, filtered, and evaporated under reduced pressure. The material was purified by column chromatography (eluent: DCM to 5% MeOH/DCM). Product containing fractions were, pooled, and reduced *in vacuo* to give 10.7 mg (27%) of **16**. MS (ES+) *m/z* 430.8 $(M + H)^+$

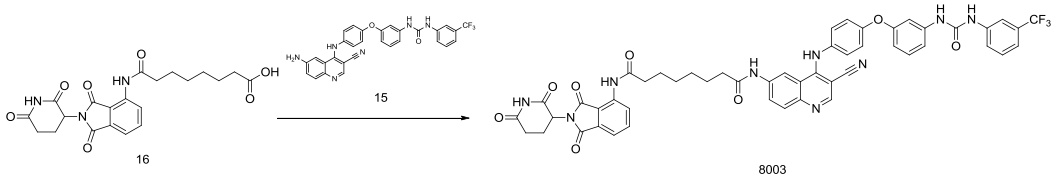

N1-(3-cyano-4-((4-(3-(3-(3-(trifluoromethyl)phenyl)ureido)phenoxy)phenyl)amino)quinolin-6-yl)-N8-(2-(2,6-dioxopiperidin-3-yl)-1,3-dioxoisoindolin-4-yl)octanediamide (**8003**). **8003** was obtained in 13% yield from **16** and **15** by a method similar to the one described for **12.** MS (ES+) *m/z* 966.8 (M + H)

References

1.Davis, M. I. *et al.* Comprehensive analysis of kinase inhibitor selectivity. *Nature Biotechnology* **29,** 1046–1051 (2011).

2.Littlefield, P., Moasser, M. M. & Jura, N. An ATP-competitive inhibitor modulates the allosteric function of the HER3 pseudokinase. *Chemistry & Biology* **21,** 453–458 (2014).

3.Taylor, S. S. & Kornev, A. P. Protein kinases: evolution of dynamic regulatory proteins. *Trends Biochem Sci* **36,** 65–77 (2010).

4.Mendez, A. S. *et al.* Endoplasmic reticulum stress-independent activation of unfolded protein response kinases by a small molecule ATP-mimic. *Elife* **4,** (2015).

5.Wang, L. *et al.* Divergent allosteric control of the IRE1α endoribonuclease using kinase inhibitors. *Nature Chemical Biology* **8,** 982–989 (2012).

6.Mi, L.-Z. *et al.* Simultaneous visualization of the extracellular and cytoplasmic domains of the epidermal growth factor receptor. *Nature Structural & Molecular Biology* **18,** 984 (2011).

7.Dar, A. C., Lopez, M. S. & Shokat, K. M. Small Molecule Recognition of c-Src via the Imatinib-Binding Conformation. *Chemistry & Biology* **15,** 1015 (2008).

8.Shi, F., Telesco, S. E., Liu, Y., Radhakrishnan, R. & Lemmon, M. A. ErbB3/HER3 intracellular domain is competent to bind ATP and catalyze autophosphorylation. *Proceedings of the National Academy of Sciences* **107,** 7692 (2010).

9.Shi, F., Telesco, S. E., Liu, Y., Radhakrishnan, R. & Lemmon, M. A. ErbB3/HER3 intracellular domain is competent to bind ATP and catalyze autophosphorylation. *Proceedings of the National Academy of Sciences* **107,** 7692 (2010).

10.Wissner, A. *et al.* 4-Anilino-6,7-dialkoxyquinoline-3-carbonitrile inhibitors of epidermal growth factor receptor kinase and their bioisosteric relationship to the 4-anilino-6,7-dialkoxyquinazoline inhibitors. *Journal of Medicinal Chemistry* **43,** 3244–3256 (2000).

11.Okaniwa, M. *et al.* Design and synthesis of novel DFG-out RAF/vascular endothelial growth factor receptor 2 (VEGFR2) inhibitors. 1. Exploration of [5,6]-fused bicyclic scaffolds. *Journal of Medicinal Chemistry* **55,** 3452–3478 (2012).

12.Wissner, A. *et al.* Synthesis and structure-activity relationships of 6,7-disubstituted 4-anilinoquinoline-3-carbonitriles. The design of an orally active, irreversible inhibitor of the tyrosine kinase activity of the epidermal growth factor receptor (EGFR) and the human epidermal growth factor receptor-2 (HER-2). *Journal of Medicinal Chemistry* **46,** 49–63 (2002).

Publishing Agreement

It is the policy of the University to encourage the distribution of all theses, dissertations, and manuscripts. Copies of all UCSF theses, dissertations, and manuscripts will be routed to the library via the Graduate Division. The library will make all theses, dissertations, and manuscripts accessible to the public and will preserve these to the best of their abilities, in perpetuity.

I hereby grant permission to the Graduate Division of the University of California, San Francisco to release copies of my thesis, dissertation, or manuscript to the Campus Library to provide access and preservation, in whole or in part, in perpetuity.

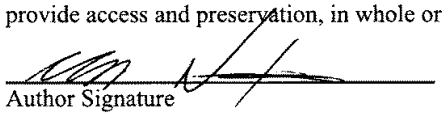

Author Signature

8/27/2016

Date